Control Engineering Practice 169 (2026) 106790

Contents lists available at ScienceDirect

Control Engineering Practice

journal homepage: www.elsevier.com/locate/conengprac

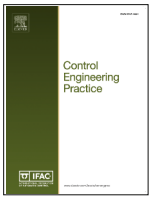

Non-minimum-phase resonant controller for active damping control: Application to piezo-actuated nanopositioning system

Aditya Natu *, Hassan Hosseinnia

Department of Precision and Microsystems Engineering, Delft University of Technology, Mekelweg 2, Delft, 2628 CD, The Netherlands

ARTICLE INFO

Keywords:
Nanopositioning
Piezo-actuated
Active damping control
Non-minimum-phase
Resonant control
Dual closed-loop

ABSTRACT

Nanopositioning systems frequently encounter limitations in control bandwidth due to their lightly damped resonance behavior. This paper presents a novel Non-Minimum-Phase Resonant Controller (NRC) aimed at active damping control within dual closed-loop architectures, specifically applied to piezo-actuated nanopositioning systems. The control strategy is structured around formulated objectives for shaping sensitivity functions to meet predetermined system performance criteria. Leveraging non-minimum-phase characteristics, the proposed NRC accomplishes complete damping and the bifurcation of double resonant poles at the primary resonance peak through a constant-gain design accompanied by tunable phase variation. The NRC demonstrates robustness against frequency variations of the resonance arising from load changes and is also capable of damping higher-order flexural modes simultaneously. Furthermore, by establishing high gains at low frequencies within the inner closed-loop and integrating it with a conventional PI tracking controller, the NRC achieves substantial dual closed-loop bandwidths that can exceed the first resonance frequency. Moreover, the NRC significantly diminishes the effect of low-frequency reference signals on real feedback errors while effectively rejecting disturbances proximate to the resonance frequency. All contributions are thoroughly formulated and exemplified mathematically, with the controller's performance confirmed through an experimental setup utilizing an industrial nanopositioning system. The experimental results indicate dual closed-loop bandwidths of 830 Hz and 755 Hz, characterized by ± 3 dB and ± 1 dB bounds, respectively, that surpass the resonance frequency of 710 Hz.

1. Introduction

Nanopositioning stages are employed for high-resolution positioning tasks, ranging from subnanometers to a few hundred micrometers (Fleming & Leang, 2014). These systems find applications in various fields, including scanning probe microscopy (SPM) (Clayton & Devasia, 2009; Shan & Leang, 2013; Tuma et al., 2013), imaging using atomic force microscopy (AFM) (Maroufi et al., 2014; Rana et al., 2014; Yong et al., 2012a), wafer and mask alignment in lithography (Lan et al., 2007; Li et al., 2006), and even micro/nano-manipulation in biological processes such as DNA sequencing (Hyun et al., 2013).

Depending on the specific task within an application, nanopositioning systems are required to track various types of references, such as periodic or arbitrary signals. However, all require a fast response to the controlled inputs. To ensure accurate reference tracking, these systems typically employ sensor-based feedback control architectures that mitigate errors arising from excited system dynamics or external disturbances (Devasia et al., 2007). In response to the growing demands for higher throughput and resolution, often exceeding the sub-nanometer level, considerable emphasis has been placed over the past two decades on designing optimized systems and closed-loop control architectures to maximize control bandwidth (Chen et al., 2021; Gu et al., 2014; Huang et al., 2024; Yong et al., 2012b).

Section 1.1 provides an overview of the typical system design and the associated challenges. Section 1.2 offers a concise overview of the various control approaches developed in the state-of-the-art to address these challenges. Finally, Section 1.3 outlines the contributions made in this work, which will form the foundation of this paper.

1.1. System design architecture and dynamics

As illustrated in Fig. 1, typical single-degree-of-freedom nanopositioning stages comprise a moving platform displaced laterally by the force generated by the actuator. Most of these stages employ piezoelectric stack actuators because of their advantageous properties, such as generating large forces, high stiffness, bandwidth, and resolution. The design integrates parallel flexures as a guiding mechanism for the platform, providing several benefits, including zero backlash and

* Corresponding author.
E-mail address: a.m.natu@tudelft.nl (A. Natu).

https://doi.org/10.1016/j.conengprac.2026.106790
Received 7 August 2025; Received in revised form 8 December 2025; Accepted 12 January 2026
Available online 22 January 2026

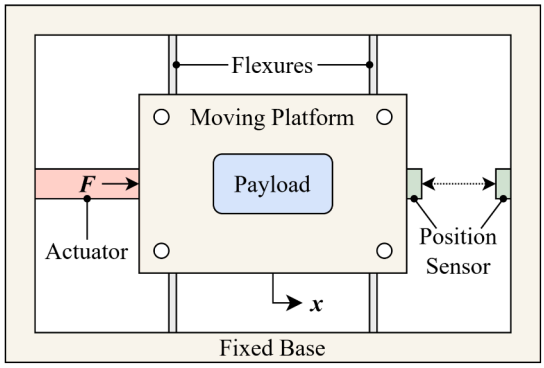

Fig. 1. A system design schematic of piezo-actuated nanopositioners.

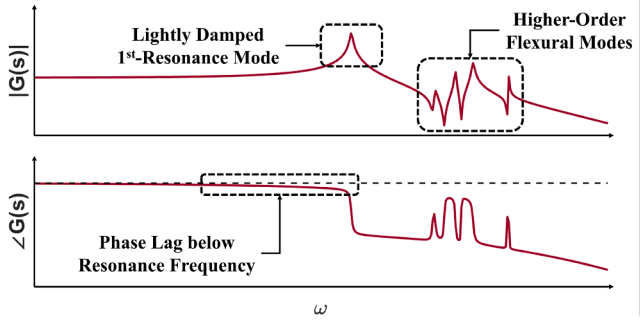

Fig. 2. Schematic of the typical frequency response of a piezo-actuated nanopositioning system.

frictionless operation. To measure platform displacement, position sensors, such as dual-plate capacitive sensors, are employed, where the capacitive change due to the platform's movement produces an output voltage, which for a few micrometers the range of motion is highly linear (Fleming & Leang, 2014).

To enable high control bandwidths, the design specification of nanopositioning stages is to have a very high first resonance frequency (ω_n) in the actuation direction, which can be obtained by highly stiff stage-guiding flexures (k_s). However, this inevitably results in a much shorter range of motion ($r \propto 1/k_s$) (Yong et al., 2012a). Thus, this often leads to a trade-off in which the stiffness of the guiding flexures, made of materials with an inherent low structural damping coefficient ($\zeta_n \approx 0.01$), is compromised to produce a sufficient travel range. The typical mass-spring-damper configuration of the stages is represented by second-order frequency dynamics:

$$G(s) = \frac{g\omega_n^2}{s^2 + \eta_n s + \omega_n^2}, \tag{1}$$

where, $s = i\omega$ denotes the Laplace variable, with i and ω being the imaginary number and frequency, respectively, and $\eta_n = 2\zeta_n\omega_n$.

The flexures also exhibit additional bending modes, observable by the sensor, which leads to the appearance of higher-order modes in the system frequency response, as illustrated in Fig. 2, which, if excited by the high-frequency components of the reference signal, will further deteriorate the positioning accuracy. Additionally, voltage amplifiers are often employed in conjunction with the stage to drive the actuators with high voltages, resulting in a low-pass filtering effect due to the series configuration of the piezo-actuator's capacitance with the amplifier's input resistance. In addition, the need for high-resolution analog-to-digital conversion (A/D) and filtering for capacitive sensor signals to achieve sub-nano resolution digital displacement signals inevitably results in a significant delay (San-Millan et al., 2015). Consequently, the system exhibits substantial phase lag within the frequency range of interest ($\omega < \omega_n$). Therefore, a general representation of the system

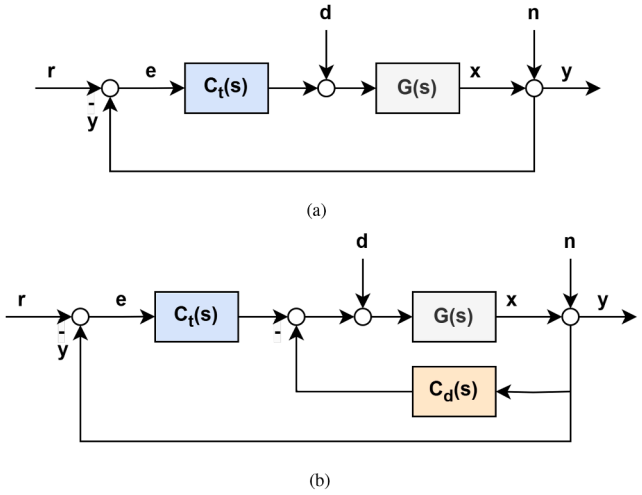

Fig. 3. (a) Conventional feedback control architecture, (b) Dual closed-loop control architecture incorporating active damping control.

dynamics is represented by:

$$G_f(s) = \left(\underbrace{\frac{\omega_n^2}{s^2 + \eta_n s + \omega_n^2}}_{\substack{\text{Dominant} \\ \text{Resonant Dynamics}}} + \underbrace{\sum_{m=2}^{N} \frac{\omega_m^2}{s^2 + \eta_m s + \omega_m^2}}_{\substack{\text{Higher-Order} \\ \text{Mode Dynamics}}} \right) \underbrace{\frac{g \cdot \omega_a}{s + \omega_a}}_{\substack{\text{Actuator} \\ \text{Amplifier} \\ \text{Dynamics}}} \underbrace{e^{-\tau s}}_{\text{Delay}}, \tag{2}$$

where, m represents the higher-order modes, $\omega_a = R \cdot C$, with R being the amplifier input impedance and C being actuator capacitance, g is the amplifier gain, and τ is the time delay.

1.2. State-of-the-art feedback-control methods

Conventionally, simple linear proportional-integral (PI) controllers have been primarily utilized to track references in a sensor-based feedback control architecture, as presented in Fig. 3(a). However, the bandwidth that such controllers can achieve is severely limited to less than 2% of the dominant resonance frequency of the system due to the highly low-damped nature of the system resonance peak (Fleming, 2009). To overcome this limitation, inversion techniques, such as notch filters, are often combined with tracking controllers to suppress the resonant dynamics, allowing for a higher bandwidth (Abramovitch et al., 2008; Feng et al., 2017). However, implementing such filters requires a very accurate representation of the system model and proves to be highly sensitive to variations in the system dynamics due to changing payload mass.

Alternatively, active damping control has been researched and developed, where damping control is implemented in an inner feedback loop within a dual-loop architecture, as illustrated in Fig. 3(b). Different techniques, including positive position feedback (PPF) (Li et al., 2015; Moon et al., 2017), integral resonant control (IRC) (Al-Mamun et al., 2013; Fleming et al., 2009), resonant control (RC) (Das et al., 2014; Ling et al., 2019), positive velocity and position feedback (PVPF) (Russell et al., 2015), positive acceleration, velocity, and position feedback (PAVPF) (Babarinde et al., 2019; Li et al., 2017), integral force feedback (IFF) (Fleming, 2009; Teo et al., 2014), etc., have been shown to provide good damping performance with modest insensitivity to variations in resonance frequency. However, for instance, in PPF, an arbitrary configuration of the resonant poles cannot be realized in the s-plane while ensuring stability. IFF requires the addition of force sensors, etc. (Feng et al., 2022). In IRC, if designed to consider model uncertainty in the control design, the system robustness needs to be improved (Feng et al., 2023). Additionally, when the system, damped with most

of these methods, is included in an integral tracking loop to obtain high gains for reference tracking, the system is still limited by a low gain margin (Fleming, 2009). In summary, these low-order fixed-structure controllers are minimum-phase, with inherent gain-phase coupling that constrains damping performance in order to maintain closed-loop stability. Advanced strategies such as H_∞ control or adaptive model-matching techniques can provide improved damping performance under uncertainties; however, they are typically associated with high-order transfer functions, which increase complexity and pose challenges for high-sampling-rate implementation, low computational cost, and practical hardware deployment (Chen et al., 2021).

1.3. Research contributions

The paper initially formulates objectives and guidelines to shape desired sensitivity functions in dual closed-loop control architectures. In line with these, this paper presents a novel non-minimum phase resonant controller (NRC) for active damping control with application to a piezo-actuated nanopositioning system. The main contributions of this work are as follows.

1. The controller leverages the characteristics of a non-minimum phase system to enable a constant-gain controller with tunable phase variation to dampen the first resonance peak completely. Additionally, the controller not only dampens the double resonant poles but also effectively splits them in the frequency domain. These aspects are discussed in detail in Sections 3 and 3.1.
2. The controller's damping performance, tuned for the unloaded system, is robust to variations in the system's resonance frequency due to load variations and ensures complete damping of resonant poles. This is demonstrated in Section 3.2.
3. The controller, aimed at damping the dominant resonance peak, is also capable of sufficiently damping the higher-order flexural modes of the system. This is formulated in Section 3.3.
4. The controller facilitates the creation of low-frequency high gains in the inner closed loop. In conjunction with a standard PI tracking controller, it enables the achievement of high closed-loop bandwidths, characterized by both ±1 dB and ±3 dB crossings, which can also exceed the system's first resonance frequency. This aspect is detailed in Section 4.2.
5. The proposed NRC, in dual closed-loop control architecture, reduces the contribution of the low-frequency reference to the real feedback errors accumulated in the system while effectively rejecting disturbances around the resonance frequency. This is also discussed in Section 4.2.

The rest of the paper is outlined as follows: Section 2 presents a perspective on sensitivity shaping for general dual closed-loop control architectures, Section 3 presents the proposed NRC for active damping control with tuning guidelines, robustness to load variations, multimode damping and high-frequency taming. Section 4 presents the combination of NRC with a conventional PI tracking controller and its tuning for desired dual closed-loop performance requirements. Section 5 presents the experimental setup and results with the proposed method, which demonstrate compliance with the analytical study and show improvement over standard methods. Finally, Section 6 concludes this paper.

2. Dual closed-loop control architecture

In conventional closed-loop structures, as illustrated in Fig. 3(a), the sensitivity of the system output has been extensively analyzed in the literature, demonstrating its correlation with closed-loop performance under various system inputs (Schmidt et al., 2020). Within the dual closed-loop control architecture that incorporates active damping, it is imperative to understand how the sensitivity functions evolve and can be delineated. In this section, the sensitivity functions are specified for a general dual closed-loop control architecture (Fig. 3(b)), relating the measured and actual positions (Sections 2.1 and 2.2, respectively). Moreover, based on general dual closed-loop performance objectives, guidelines for shaping these sensitivities are provided in Section 2.3.

2.1. Redefined sensitivities

The primary variables that serve as input within the system include the reference r, the process disturbance d, and the output disturbance n. Sensor noise within the measurement system is incorporated into n, thus characterizing the system output y as the measured output.

The damping controller $C_d(s)$ and the tracking controller $C_t(s)$ collaboratively enhance bandwidth in the dual closed-loop system. In Fig. 3(b), the dual closed-loop transfer function $T_{yr}(s)$, mapped from reference r to position output y, is given by:

$$T_{yr}(s) = \frac{G(s)C_t(s)}{1 + G(s)\big(C_t(s) + C_d(s)\big)}. \tag{3}$$

The dual closed-loop transfer function $S_{yn}(s)$, widely known as the sensitivity function, mapping from the output disturbance n to the measured output y can be expressed as:

$$S_{yn}(s) = \frac{1}{1 + G(s)\big(C_t(s) + C_d(s)\big)}. \tag{4}$$

Subsequently, the dual closed-loop transfer function $PS_{yd}(s)$, known as the process sensitivity function, mapping from the process disturbance d to the measured output y can be expressed as:

$$PS_{yd}(s) = \frac{G(s)}{1 + G(s)\big(C_t(s) + C_d(s)\big)}. \tag{5}$$

Dual closed-loop functions in (3) and (4) lack complementarity, unlike standard feedback architectures. By examining the interaction between the tracking and damping controllers, control strategies can be optimized for reference tracking, disturbance rejection, and noise attenuation.

2.2. Real feedback error sensitivity

The three dual closed-loop functions defined in Section 2.1 depict the impact of any of the inputs on the measured output y. However, in reality, the actual positioning error $e_r = r - x$ is of greater interest and importance than the control error $e = r - y$, where x is the actual or real position of the system (Schmidt et al., 2020). Thus, it is worthwhile to investigate how the real error e_r maps to different inputs in the system to understand and compute the contribution of each of these inputs to the real error. Since e_r is concerned with the x, the dual closed-loop transfer functions mapping from the inputs r, d, and n to x are first defined as follows:

$$T_{xr}(s) = \frac{G(s)C_t(s)}{1 + G(s)\big(C_t(s) + C_d(s)\big)} = T_{yr}(s). \tag{6}$$

$$PS_{xd}(s) = \frac{G(s)}{1 + G(s)\big(C_t(s) + C_d(s)\big)} = PS_{yd}(s). \tag{7}$$

$$S_{xn}(s) = \frac{-G(s)\big(C_t(s) + C_d(s)\big)}{1 + G(s)\big(C_t(s) + C_d(s)\big)} \neq S_{yn}(s). \tag{8}$$

According to (4) and (8), the primary distinction becomes evident in the dual closed-loop sensitivity function concerning input n. Consequently, x can be articulated as:

$$x = T_{xr}(s)r + PS_{xd}(s)d + S_{xn}(s)n. \tag{9}$$

Using linear time-invariant system theory and applying a statistical addition assuming that the signals r, d, and n are uncorrelated, e_r can

be expressed as (Schmidt et al., 2020):

$$
\begin{aligned}
e_r^2 =& (r-x)^2 \\
=& \left(\frac{(r-x)}{r}r\right)^2 + \left(\frac{(r-x)}{d}d\right)^2 + \left(\frac{(r-x)}{n}n\right)^2 \\
=& \left(1-T_{xr}(s)\right)^2 r^2 + \left(PS_{xd}(s)\right)^2 d^2 + \left(S_{xn}(s)\right)^2 n^2 \\
=& \left(\underbrace{\frac{1+G(s)C_d(s)}{1+G(s)\left(C_t(s)+C_d(s)\right)}}_{T'_{xr}(s)}\right)^2 r^2 \\
& \left(\frac{G(s)}{1+G(s)\left(C_t(s)+C_d(s)\right)}\right)^2 d^2 + \\
& \left(\frac{-G(s)\left(C_t(s)+C_d(s)\right)}{1+G(s)\left(C_t(s)+C_d(s)\right)}\right)^2 n^2 \Longrightarrow \\
e_r =& \sqrt{\left(T'_{xr}(s)r\right)^2 + \left(PS_{xd}(s)d\right)^2 + \left(S_{xn}(s)n\right)^2}.
\end{aligned}
\tag{10}
$$

Note: It should be emphasized that in such dual closed-loop control architectures, the pairs of transfer functions $T_{yr}(s) = T_{xr}(s)$, $T'_{xr}(s)$, and $S_{yn}(s)$, $S_{xn}(s)$ are complementary functions.

2.3. Shaping sensitivities for dual closed-loop control

The objectives of the dual closed-loop control system can be formulated in the frequency domain by defining the desired shapes of the closed-loop and open-loop transfer functions. Although loop-shaping guidelines have been presented in the literature for independently tracking controllers and damping controllers (Dastjerdi et al., 2018; Kaczmarek & HosseinNia, 2023; Wang & Chen, 2017), we focus on the interaction of these two in a dual closed-loop architecture. As established in 2.2, what actually matters is to look at the real error feedback sensitivity functions, namely $T'_{xr}(s)$, $PS_{xd}(s)$, and $S_{xn}(s)$, and reduce their contributions to e_r in the system. Thus, in this section, the objectives to shape the dual closed-loop transfer functions and, subsequently, the tracking ($C_t(s)$) and damping ($C_d(s)$) controllers will be presented.

Note: Three notation to be used are defined as follows:

- Dual Closed-Loop Control Bandwidth ω_c

$$\omega_c := \{\omega \in \mathbb{R} \mid \omega \geq 0 \text{ and } |T_{xr}(s)|_{\omega>\omega_c} < 1\}. \tag{11}$$

- Tracking Controller Frequency ω_{C_t}

$$\omega_{C_t} := \{\omega \in \mathbb{R} \mid \omega \geq 0 \text{ and } |C_t(s)|_{\omega<\omega_{C_t}} \gg 1\}. \tag{12}$$

- Dual Open Loop $L_D(s)$

$$L_D(s) := G(s)(C_t(s) + C_d(s)). \tag{13}$$

The dual closed-loop shaping objectives and the guidelines to achieve them are discussed below:

1. *O_1: Maximizing Dual Closed-Loop Control Bandwidth*
   The system should be able to track references ($x \approx r$) up to as high frequencies as possible. Due to the complementary nature of $T_{xr}(s)$ and $T'_{xr}(s)$, it also results in low real errors due to reference signals. The objective can thus be defined as:

$$\max \omega_c \Big| \; |T'_{xr}(s)| \approx 0 \Leftrightarrow |T_{xr}(s)| \approx 1 \;\forall\; \omega \leq \omega_c. \tag{14}$$

   This is achieved by ensuring $|G(s)C_d(s)| = 1$ and $\angle G(s)C_d(s) = \pm\pi \;\forall\; \omega < \omega_c$ (10). Thus, $|C_d(s)| \;\forall\; \omega < \omega_c$ should be a constant gain equal to $|G^{-1}(0)|$ as $|G(s)| = |G(0)| \;\forall\; \omega < \omega_n$.

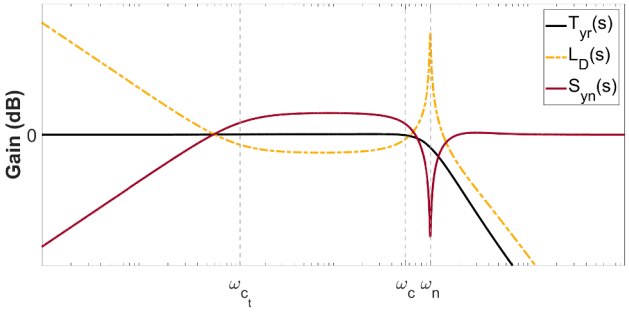

Fig. 4. Illustration of the dual closed-loop shaping for a 2nd-order lightly-damped system.

2. *O_2: Maximizing Low-Frequency Disturbance Rejection*
   The system should be able to minimize the influence of low-frequency disturbances on the real error, implying a good disturbance rejection performance. The objective can thus be defined as:

$$\begin{aligned}\max \omega_{C_t} \Big| \; & |PS_{xd}(s)| \ll |G(s)| \;\forall\; \omega < \omega_{C_t} \\ & \Leftrightarrow |S_{yn}(s)| \ll 1 \;\forall\; \omega < \omega_{C_t}.\end{aligned} \tag{15}$$

   Taking into account O_1, this is achieved by ensuring $|C_t(s)|_{\omega<\omega_{C_t}} \gg 1$.
3. *O_3: Maximizing Active Damping Performance*
   The system resonance peak should be damped as much as possible to enable higher control bandwidths and to avoid excessive excitation of disturbances at that frequency. The objective can thus be defined as:

$$\begin{aligned}\max |L_D(s)|_{\omega=\omega_n} \Big| \; & |PS_{xd}(s)| \ll |G(s)| \text{ at } \omega = \omega_n \\ & \Leftrightarrow |S_{yn}(s)| \ll 1 \text{ at } \omega = \omega_n.\end{aligned} \tag{16}$$

   This is achieved by ensuring $|L_D(s)|_{\omega=\omega_n} \gg 1$ and preferably $\angle L_D(s)_{\omega=\omega_n} \approx \pm\pi$.
4. *O_4: Maximizing Noise Attenuation Performance*
   The system should be able to minimize the influence of high-frequency noise on real error, implying good noise attenuation performance. The objective can thus be defined as:

$$\begin{aligned}\min |L_D(s)|_{\omega\gg\omega_n} \Big| \; & |S_{xn}(s)| \approx 0 \;\forall\; \omega \gg \omega_n \\ & \Leftrightarrow |S_{yn}(s)| \approx 1 \;\forall\; \omega \gg \omega_n.\end{aligned} \tag{17}$$

   This is achieved by ensuring $|L_D(s)|_{\omega\gg\omega_n} \ll 1$. Thus, $|C_t(s)| \ll 1$ and $|C_d(s)| \ll 1 \;\forall\; \omega \gg \omega_n$.

For dual closed-loop stability, there should be a sufficient phase margin ϕ_{m_i} at all three crossover frequencies $\omega_{cf_i} \Big| \; |L_D(\omega_{cf_i})| = 1;\; i = \{1,2,3\}$.

However, there are some fundamental limitations with such a linear dual closed-loop control system, as discussed below.

1. The frequencies (ω_{C_t}) up to which the tracking controllers have high gains cannot be pushed to be arbitrarily large. From a stability perspective, the dual closed-loop control system should have sufficient stability margins to ensure robustness. Typically, high gains are obtained using integrators, where increasing integrator frequency ($\omega_i \approx \omega_{C_t}$) adversely affects stability margins. From a hardware perspective, the control inputs to the actuators cannot be arbitrarily high and fast due to the saturation and bandwidths of the actuators (Wang & Chen, 2017).
2. While maximizing the reference tracking performance by maximizing the dual closed-loop control bandwidth (ω_c) ensures minimal real error accumulation due to references ($|T'_{xr}(s)| \approx 0$) in the frequency regime of interest ($\omega \leq \omega_c$), it results in an inevitable trade-off of error accumulation due to noise ($|S_{xn}(s)| \approx 1$). This fundamental limitation, known as the waterbed effect, transpires from Bode's integral theorem (Schmidt et al., 2020).

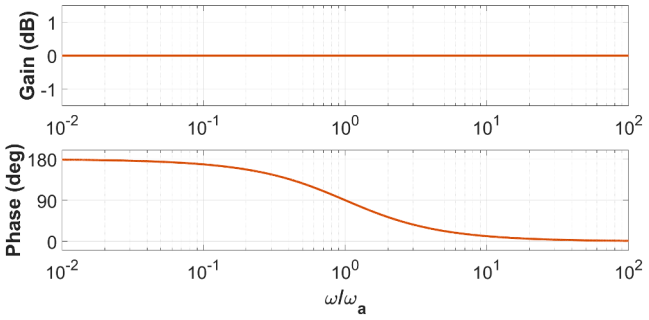

Fig. 5. Frequency response of Non-Minimum Phase Resonant Controller $C_d(s)$ for $k = 1$.

Fig. 4 elucidates the concept of dual closed-loop shaping objectives and limitations, as previously delineated. Although the state-of-the-art damping controllers introduced in 1.2 adhere to this dual closed-loop shaping framework, their performance is restricted due to the interdependence of their gain and phase. Recognizing this, the present paper introduces and implements a novel active damping controller characterized by a constant-gain design and a tunable phase. This approach upholds the dual closed-loop shaping guidelines, exceeds the performance of existing state-of-the-art methods, and exemplifies the contributions presented in 1.3.

3. Non-minimum-phase resonant controller (NRC)

In this section, we present a novel Non-Minimum-Phase Resonant Controller (NRC) for active damping control, described by the transfer function:

$$C_d(s) = k \cdot \left(\frac{s-\omega_a}{s+\omega_a}\right), \tag{18}$$

where ω_a signifies the tuned corner frequency of the controller, and k represents the controller's gain. Fig. 5 illustrates the frequency domain plot of the described controller. A distinctive characteristic of this controller is its constant gain across all frequencies, which is expressed as:

$$\left|C_d(j\omega)\right| = k \quad \forall\ \omega \in [0, \infty). \tag{19}$$

The phase response of the controller is defined as:

$$\angle C_d(j\omega) = -2\tan^{-1}\left(\frac{\omega}{\omega_a}\right). \tag{20}$$

Notably, the phase of the controller transitions from 180° to 0° as the frequency varies from 0 to $2\omega_a$, and provides the −90° phase at ω_a. The controller consists of one pole in the left half-plane (LHP) at $s = -\omega_a$ and a zero in the right half-plane (RHP) at $s = \omega_a$, resulting in a non-minimum-phase characteristic.

3.1. Active damping control with NRC

Active damping is implemented by placing the proposed NRC in a negative feedback loop, as illustrated in Fig. 3(b).

The controller parameters are parameterized in terms of the general system model (1) to facilitate an easy tuning process. The controller corner frequency is expressed as $\omega_a = n\omega_n$, where n represents the normalized corner frequency with respect to the natural frequency of the plant:

$$n = \frac{\omega_a}{\omega_n}. \tag{21}$$

The controller gain k is defined as

$$k = \gamma|G(s)|^{-1}_{s=0} = \gamma g^{-1} \quad \forall\ \gamma \in (0, 1], \tag{22}$$

such that the loop DC gain follows $0 < |G(s)C_d(s)|_{s=0} \leq 1$, ensuring closed-loop stability, as detailed later.

The inner closed-loop transfer function from the input disturbance d to the system output y can be formulated as

$$\begin{aligned} G_d(s) &= \frac{G(s)}{1 + G(s)C_d(s)} \\ &= \frac{g\omega_n^2\left(s + n\omega_n\right)}{s^3 + \left(n\omega_n + 2\zeta_n\omega_n\right)s^2 + \left(2\zeta_n n\omega_n^2 + (1+\gamma)\omega_n^2\right)s + n(1-\gamma)\omega_n^3}. \end{aligned} \tag{23}$$

The inner closed-loop characteristic equation thus comprises three poles ($p_{1,2,3}$) and one zero (z_1). For any $\omega_a > 0$, z_1 lies in the LHP, ensuring minimum-phase behavior of the closed-loop function $G_d(s)$.

The NRC parameters (k, ω_a) influence the frequency response characteristics of the inner closed loop. The DC gain of $G_d(s)$ is given by

$$|G_d(s)|_{s=0} = \frac{g}{1-\gamma}. \tag{24}$$

3.1.1. Inner closed-loop stability

The characteristic equation for the inner closed loop is given by

$$s^3 + \left(n\omega_n + 2\zeta_n\omega_n\right)s^2 + \left(2\zeta_n n\omega_n^2 + (1+\gamma)\omega_n^2\right)s + n(1-\gamma)\omega_n^3 = 0. \tag{25}$$

The stability conditions can be determined by applying the Routh-Hurwitz criterion to (25). The first two rows of the Routh-Hurwitz array are filled with these coefficients as follows:

$$\begin{array}{c|cc} s^3 & 1 & 2\zeta_n n\omega_n^2 + (1+\gamma)\omega_n^2 \\ s^2 & n\omega_n + 2\zeta_n\omega_n & n(1-\gamma)\omega_n^3 \\ s^1 & \frac{\omega_n^2(2\zeta_n n^2 + 2\gamma n + 4\zeta_n^2 n + 2\zeta_n(1+\gamma))}{n+2\zeta_n} & 0 \\ s^0 & n(1-\gamma)\omega_n^3 & 0. \end{array} \tag{26}$$

To ensure stability, the first column of the Routh array must be positive (Åström & Murray, 2021). For $n, \omega_n, \zeta_n, \gamma > 0$, the first three terms are always positive based on (26). Hence, the following condition must be satisfied for the fourth term:

$$(1-\gamma)n\omega_n^3 > 0, \tag{27}$$

and (22) and (27) together imply that stability is preserved for $0 < \gamma < 1$.

Marginal stability for $\gamma = 1$: If the controller gain k exactly inverts the system DC gain ($k = g^{-1}$), one root of the characteristic equation (25) is at $s = 0$, similar to that of a pure integrator, making the closed loop marginally stable.

3.1.2. Tuning NRC gain

From the inner closed loop function (23), it is evident that tuning γ strongly influences the frequency response characteristics of the inner closed loop. Motivated by the dual closed-loop shaping guideline (15), presented in Section 2.3, to reduce the effect of the input reference r on the real error e_r, γ is tuned to unity such that $|G(s)C_d(s)| = 1$ and $\angle G(s)C_d(s) = \pi$ for $\omega \ll \omega_a$.

As established in Section 3.1.1, tuning $\gamma = 1$ results in a pole located at $s = 0$, yielding marginal stability. However, it will be shown later in Section 4.1.1 that the tracking controller $C_t(s)$ in the outer loop can be tuned to guaranty sufficient stability margins.

Fig. 6 illustrates the inner closed-loop magnitude response as the normalized controller frequency n varies for the NRC tuned with $\gamma = 1$. It can be deduced that, for a fixed γ, the controller frequency ω_a must be further tuned to achieve inner closed-loop damped poles.

3.1.3. Tuning NRC corner frequency

Here, the achievable closed-loop damping is evaluated as a function of ω_a for the gain condition established in Section 3.1.2. For $\gamma = 1$, the three poles of $G_d(s)$ are located at

$$\begin{aligned} p_1 &= 0, \\ p_{2,3} &= \frac{-\left(2\zeta_n\omega_n + n\omega_n\right) \pm \sqrt{\left(2\zeta_n\omega_n + n\omega_n\right)^2 - 4\left(2\zeta_n n\omega_n^2 + 2\omega_n^2\right)}}{2}. \end{aligned} \tag{28}$$

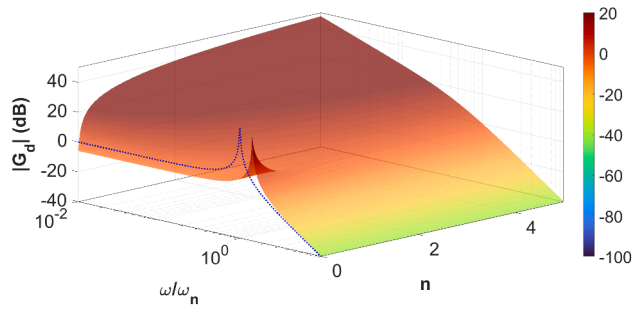

Fig. 6. Frequency response magnitude $|G_d(s)|$ vs. n for $\gamma = 1$. The dashed blue line depicts $|G(s)|$.

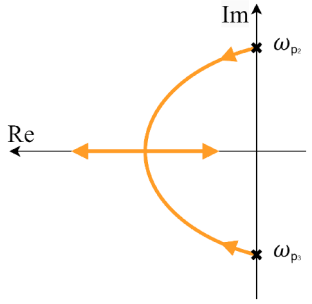

Fig. 7. Root locus schematic of inner closed-loop double resonant poles $p_{2,3}$.

From (28), it can be deduced that this specific tuning of the damping controller manifests an integrator effect in the inner closed loop by placing a pole at zero, while the locations of the remaining two poles depend on ω_a.

The primary objective of the damping controller in this study is to effectively introduce damping to the lightly damped poles inherent in the plant dynamics. This is achieved through strategic manipulation of the inner closed-loop poles, facilitating a shift towards the left-half plane (LHP) and consequently increasing the negative real part of these poles. The damping ratio ζ_d of the closed-loop double poles is characterized by

$$\zeta_d = -\cos\left(\angle p_{2,3}\right), \tag{29}$$

where $\angle p_{2,3}$ is the angle of the line connecting the pole to the origin in the s-domain, measured clockwise from the negative real axis.

Fig. 7 provides a schematic representation of the typical root locus trajectory associated with the double resonant poles $p_{2,3}$. In a lightly damped system, these poles start as complex conjugates residing in the LHP, with their real parts becoming increasingly negative as the parameter n increases. However, at a certain $n = f(\zeta_n)$, these double poles coalesce and subsequently bifurcate along the negative real axis, signifying complete damping ($\Im(p_{2,3}) = 0$). Subsequently, they follow an opposite trajectory along the real axis. Thus, the condition for completely damped poles is given by

$$n \geq 2(\sqrt{2} + \zeta_n). \tag{30}$$

Thus, for $n \gtrapprox 2\sqrt{2}$ (for a small damping ratio $\zeta_n \approx 0.01$), the double resonant poles $p_{2,3}$ can achieve complete damping. It should be noted that this condition is valid for the case $\gamma = 1$. Fig. 8 illustrates the variation in the closed-loop frequency response $G_d(s)$ as γ varies for a fixed $n = 3$.

Effect of damping ratio: Despite the dependence of the damping ratio of the damped poles ζ_d on the normalized corner frequency n, its impact remains negligible for typically lightly damped plants ($\zeta_n \approx 0.01$). Fig. 9 underscores the minimal influence exerted by the plant damping ratio on the root locus of the double resonant poles.

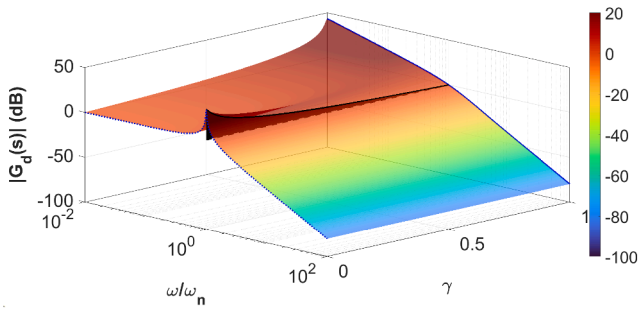

Fig. 8. Frequency response magnitude $|G_d(s)|$ vs. γ for $n = 3$. The dashed blue line depicts $|G(s)|$, the solid blue line depicts $|G_d(s)|$ when $n = 3$, and the black line traces the resonance peak magnitude $|G_d(s)|_{\omega=\omega_n}$.

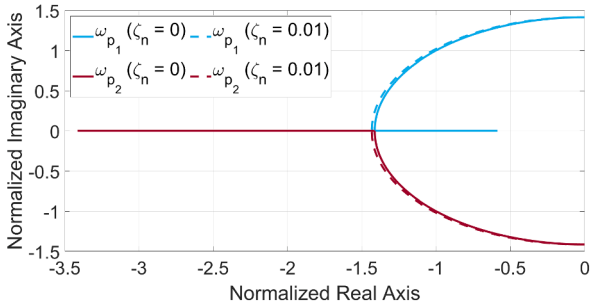

Fig. 9. Influence of plant damping on the root locus of resonant poles $p_{2,3}$.

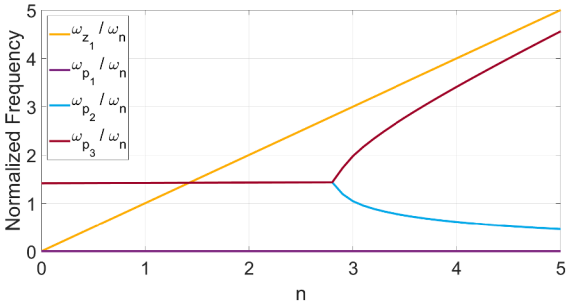

Fig. 10. Inner closed-loop poles $p_{1,2,3}$ and zero z_1 as a function of the tuned controller normalized corner frequency n.

3.1.4. *Effect of closed-loop zero*

From (23), it is evident that the inner closed-loop transfer function consists of three poles ($p_{1,2,3}$) and one zero (z_1). The phase response of the inner closed-loop system depends on the positioning of these poles and the zero within the frequency domain. Although the closed-loop zero remains fixed for a constant controller corner frequency, it was previously demonstrated that the double poles follow a specific trajectory and split as n increases. In scenarios characterized by low plant damping values, the split poles remain consistently lower in frequency than the zero frequency, with one pole situated closer to the zero frequency, as shown in Fig. 10.

The additional $-90°$ phase shift introduced by the pole at a higher frequency is approximately counteracted by the $+90°$ phase shift from the zero near its frequency. Consequently, in the absence of system delay, the inner closed-loop response transitions from $-90°$ to $-180°$ as the frequency increases. Once again, the system damping ratio has a minimal influence on the relationship between the closed-loop pole and zero frequencies. Henceforth, for the sake of mathematical convenience, the plant under consideration will be simplified as an undamped ($\zeta_n = 0$) second-order transfer function.

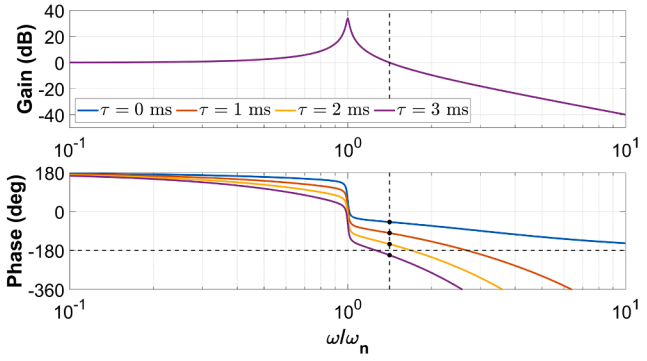

(a)

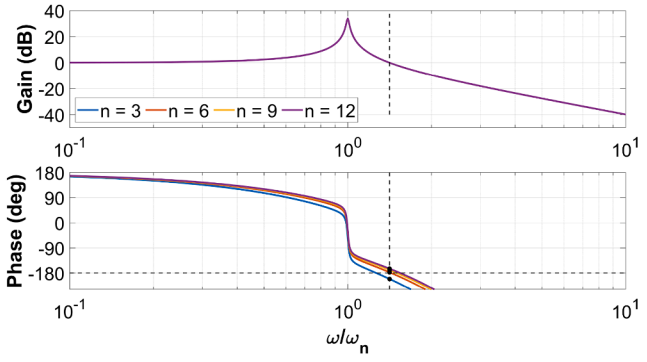

(b)

Fig. 11. Illustration of the effect of delay on inner-loop stability. (a) Open-loop frequency response $G(s,\tau)C_d(s)$ for varying time delay τ and $n = 3$, (b) open-loop frequency response $G(s,\tau)C_d(s)$ for varying n and fixed $\tau = 3$ ms.

3.1.5. Effect of delay

As discussed in Section 1.1, the dynamics of the nanopositioning system often contain significant delays that can be attributed to the extremely high resolution of the analog-to-digital conversion process and signal filtering. Thus, taking delay into account, the system dynamics can be represented as

$$G(s,\tau) = \frac{g\omega_n^2}{s^2 + 2\zeta_n\omega_n s + \omega_n^2} e^{-\tau s}, \tag{31}$$

where τ is the time delay in seconds.

To investigate the influence of delay on stability, Fig. 11(a) presents the inner open-loop response $G(s,\tau)C_d(s)$ as the time delay τ increases. Following the loop-shaping guideline presented in Kaczmarek and HosseinNia (2023), the stability condition is evaluated at the crossover frequencies defined as

$$\omega_{c_i} := \omega \mid \omega \in \mathbb{R} \text{ and } |G(j\omega_{c_i})C_d(j\omega_{c_i})| = 1, \quad i = 1,2. \tag{32}$$

Accordingly, for closed-loop stability, the open-loop system must satisfy the following phase conditions for $k \in \mathbb{Z}$ and $\omega_{c_1} < \omega_{c_2}$:

$$\begin{aligned} &\angle G(j\omega_{c_1},\tau)C_d(j\omega_{c_1}) + (2k-1)\pi \le 0, \\ &\angle G(j\omega_{c_2},\tau)C_d(j\omega_{c_2}) + (2k+1)\pi \ge 0. \end{aligned} \tag{33}$$

As shown in Fig. 11(a), for $\tau = 3$ ms, the stability condition is violated at the second crossover frequency, resulting in instability when $C_d(s)$ is tuned to the nominal value $n = 3$. To account for the delay and avoid instability, the parameter n can be increased, thereby shifting the phase lag such that the stability conditions in (33) are satisfied. Fig. 11(b) illustrates this effect, showing that higher n values enhance stability margins and consequently improve damping performance around the crossover frequency.

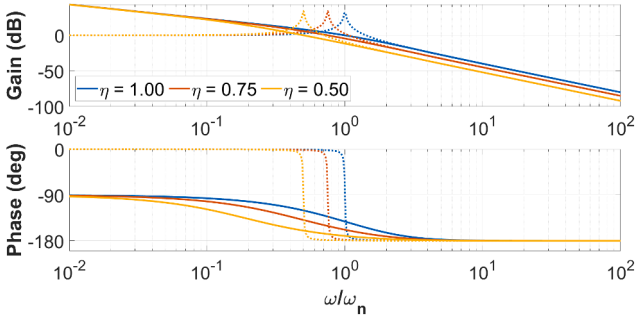

Fig. 12. Illustration of the robustness of NRC to variations in resonance frequency. Dotted lines depict $\hat{G}(s)$ and solid lines depict $\hat{G}_d(s)$.

3.2. Robustness to resonance frequency variations

Often, samples or payloads must be positioned using nanopositioning stages. The associated payload mass (m_p) changes the resonance frequency ($\omega_n \propto \sqrt{\frac{k}{m_s+m_p}}$), where k and m_s denote the flexural stiffness and the stage mass, respectively. Although typical damping controllers are tuned for the identified nominal (unloaded) system, their closed-loop damping performance can be severely affected when the resonance frequency varies significantly. In such cases, more advanced adaptive algorithms for real-time tuning are usually required (Yong et al., 2012a).

This subsection examines the robustness of NRC with respect to variations in resonance frequency. The altered frequency is denoted by $\hat{\omega}_n = \eta\omega_n$, with $\eta \in (0,1)$, and the loaded plant is modeled by $\hat{G}(s) = \frac{g\hat{\omega}_n^2}{s^2+2\zeta_n\hat{\omega}_n s+\hat{\omega}_n^2}$. For NRC tuned with $\gamma = 1$ and $\omega_a = n\omega_n$ in the unloaded state, the resulting inner closed-loop transfer function is given by

$$\hat{G}_d(s) = \frac{g\hat{\omega}_n^2\left(s + n\omega_n\right)}{s^3 + \left(n\omega_n + 2\zeta_n\hat{\omega}_n\right)s^2 + \left(2\zeta_n n\omega_n\hat{\omega}_n + 2\hat{\omega}_n^2\right)s}. \tag{34}$$

The condition for complete damping, as derived from (28) and (30), is

$$n \ge 2\eta(\sqrt{2} + \zeta_n). \tag{35}$$

Since $\eta < 1$, any n that satisfies (30) also satisfies (35). Hence, an NRC set for the nominal system achieves complete damping across the considered loaded systems, demonstrating its robustness to changes in resonance frequency. This behavior is illustrated in Fig. 12, where an NRC tuned for the unloaded case ($\eta = 1$) is used to dampen two loaded conditions ($\eta = 0.75, 0.5$).

3.3. Damping multiple resonant modes

The use of NRC to actively damp the first dominant resonance mode has been extensively discussed in Section 3.1. However, as briefly outlined in Section 1.1, higher-order modes in the vicinity of the dominant resonance mode can further deteriorate the position accuracy. This motivates the additional damping of these modes. In this subsection, we show that the NRC used for the first mode can also induce damping in significant higher-order modes in the vicinity.

For simplicity, an undamped system with two modes is considered for the analysis. Based on the theory of modal decomposition, the system $G_2(s)$ can be expressed as

$$\begin{aligned} G_2(s) &= \frac{\omega_n^2}{s^2+\omega_n^2} + \beta\frac{\omega_2^2}{s^2+\omega_2^2} \\ &= \frac{(1+\alpha^2\beta)\omega_n^2 s^2 + \alpha^2\omega_n^4(1+\beta)}{s^4 + (1+\alpha^2)\omega_n^2 s^2 + \alpha^2\omega_n^4}, \end{aligned} \tag{36}$$

where $\omega_2 > \omega_n$ is the resonance frequency of the second mode, and the factor $\beta \in (0,1)$ relates the high-frequency contribution of the second

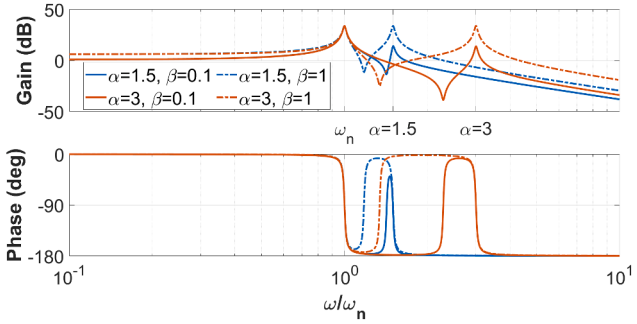

Fig. 13. Illustration of the frequency response of $G_2(s)$ as a function of α and β.

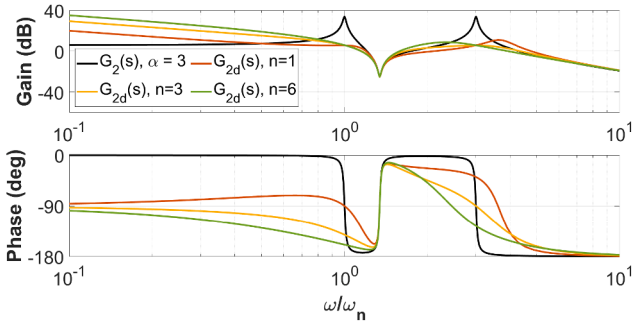

Fig. 14. Illustration of the frequency response of $G_{2d}(s)$ as n varies relative to α.

mode to that of the first mode. A parameter $\alpha > 1$ is introduced to normalize ω_2 with respect to ω_n, as $\omega_2 = \alpha\omega_n$.

The sum of the two modes leads to a double zero ω_z being created such that $\omega_n < \omega_z < \omega_2$, the location of which is given by $s = \pm i\alpha\omega_n\sqrt{\frac{1+\beta}{1+\alpha^2\beta}}$. The DC gain is $G_2(0) = 1 + \beta$. Fig. 13 illustrates the frequency response of $G_2(s)$ as the parameters α and β vary.

The inner closed-loop transfer function $G_{2d}(s)$ with an NRC tuned to damp the first resonance mode ($k = \frac{\gamma}{1+\beta}$) is symbolically computed as

$$G_{2d}(s) = \frac{((1+\alpha^2\beta)\omega_n^2 s^2 + \alpha^2\omega_n^4(1+\beta))(s+n\omega_n)}{c_5 s^5 + c_4 s^4 + c_3 s^3 + c_2 s^2 + c_1 s + c_0}$$

where,

$$\begin{aligned} c_5 &= 1;\ c_4 = n\omega_n; \\ c_3 &= ((1+\alpha^2) + k(1+\alpha^2\beta))\omega_n^2; \\ c_2 &= ((1+\alpha^2) - k(1+\alpha^2\beta))n\omega_n^3; \\ c_1 &= \alpha^2\omega_n^4(1+k(1+\beta)); \\ c_0 &= \alpha^2 n\omega_n^5(1-k(1+\beta)). \end{aligned} \tag{37}$$

The magnitude of $G_{2d}(s)$ at ω_2 is obtained by substituting $s = i\alpha\omega_n$ and simplifies to

$$|G_{2d}(s)|_{\omega=\alpha\omega_n} = \frac{1}{k} = \frac{1+\beta}{\gamma}. \tag{38}$$

When comparing (38) with $|G_2(s)|_{\omega=\alpha\omega_n} \approx \infty$ for $\zeta_n \approx 0$, the reduction in magnitude indicates that damping is achieved in the second resonance mode. However, the second resonance peak frequency $\hat{\omega}_2$ in closed loop can differ from ω_2 depending on the relation between n and α, such that (a) if $n = \alpha$, then $\hat{\omega}_2 = \omega_2$; (b) if $n < \alpha$, then $\hat{\omega}_2 > \omega_2$; and (c) if $n > \alpha$, then $\hat{\omega}_2 < \omega_2$, as illustrated in Fig. 14. It should be noted that delay in the system affects the magnitude of the induced damping, as highlighted in Section 3.1.5.

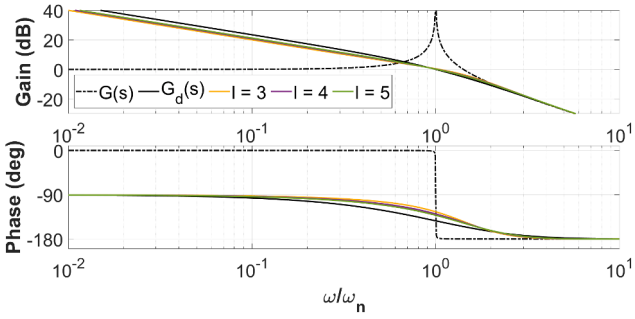

Fig. 15. Illustration of the variation in the frequency response of $G_{d_l}(s)$ as the parameter l varies. $G_d(s)$ is presented as a black solid line for comparison.

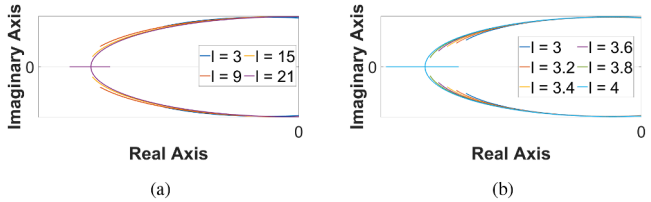

Fig. 16. Root locus trajectory of double resonant poles $p_{2,3}$ when (a) $0 \le n \le 3$ and complete damping is achieved for higher l, (b) $0 \le n \le 4.5$ and complete damping is achieved for smaller l.

3.4. Taming NRC

The NRC lacks roll-off at high frequencies owing to its constant gain characteristic. As a result, when it is augmented by the amplifier, noise is fed back into the closed-loop system, which can potentially lead to the accumulation of real errors due to the significantly higher-order modes present. Mathematically, the NRC output signal v (see Fig. 3(b)) can be represented as $v = C_d(s) \cdot y = C_d(s) \cdot (x + n)$. At high frequencies, where noise typically becomes predominant due to system roll-off ($x \approx 0$ as $\lim_{s\to\infty} G(s) = 0$), the noise entering the amplifier through the inner feedback loop can be expressed as

$$v = \lim_{s\to\infty} C_d(s) \cdot n \approx k \cdot n. \tag{39}$$

Eq. (39) emphasizes the importance of high-frequency roll-off in $C_d(s)$ to attenuate transmitted noise, if significant. Motivated by the dual closed-loop shaping guideline (17), presented in Section 2.3, the NRC can be tamed using a simple 1st-order low-pass filter to achieve $|C_d(s)| \ll 1\ \forall\ \omega \gg \omega_n$. However, such taming can affect the damping performance in the closed-loop system, depending on the filter taming frequency ω_l, as further investigated in the following. The taming frequency is parameterized by normalizing with respect to the resonance frequency as $\omega_l = l \cdot \omega_n$.

The tamed NRC filter can be expressed as

$$C_{d_t}(s) = k\left(\frac{s-\omega_a}{s+\omega_a}\right)\left(\frac{\omega_l}{s+\omega_l}\right). \tag{40}$$

Thus, the inner closed-loop transfer function of the tamed NRC (tuned for $\gamma = 1$) in feedback with a 2nd-order undamped system can be written as

$$G_{d_t}(s) = \frac{\omega_n^2(s^2 + (n+l)\omega_n s + nl\omega_n^2)}{s(s^3 + (n+l)\omega_n s^2 + (nl+1)\omega_n^2\, s + (n+2l)\omega_n^3}. \tag{41}$$

The denominator of Eq. (41) simplifies to a quartic equation with a zero constant term, introducing the 4th pole (p_4) via the taming filter. The damping of the double resonant poles ($p_{2,3}$) now depends on the parameter l. Fig. 15 shows how the inner closed-loop frequency response $G_{d_t}(s)$ varies when the tamed NRC $C_{d_t}(s)$ is tuned for $n = 3$ (30) as ω_l changes, highlighting the variation of the damping performance.

Thus, l directly affects the achievable damping performance. To ensure complete damping, n must be re-tuned based on l.

Fig. 16(a) shows the root locus trajectory of the double resonant poles when $0 \leq n \leq 3$ and l is varied. It can be observed that, for complete damping to be achieved without re-tuning n, l needs to be significantly increased. However, as illustrated in Fig. 16(b) (when $0 \leq n \leq 4.5$), if n is re-tuned to slightly higher values, complete damping can be achieved for much smaller l.

4. Dual closed-loop control based on NRC

This section presents the combination of NRC with the conventional PI tracking controller and the controller tuning in the outer loop for desired dual closed-loop performance requirements.

4.1. Motion tracking control loop

In nanopositioning systems, a tracking controller $C_t(s)$ is used to ensure accurate reference tracking. It is typically designed using loop-shaping techniques in the frequency domain. A Proportional-Integral (PI) controller is commonly employed to set the desired bandwidth and ensure zero steady-state error. Its transfer function is given by

$$C_t(s) = k_p \cdot \left(1 + \frac{\omega_i}{s}\right), \tag{42}$$

where k_p denotes the proportional gain, and ω_i represents the integrator corner frequency.

When an active damping controller is integrated in a dual closed-loop structure, as depicted in Fig. 3(b), the design of the tracking controller is typically based on the dynamics of the inner closed-loop system. In the following, the controller design process is outlined for the case where the inner loop features the NRC for active damping.

4.1.1. Proportional gain

If the inner loop provides an integrator effect, the outer tracking loop can be implemented with a proportional gain k_p only. This configuration can still achieve zero steady-state error in the dual closed-loop system, provided that the proportional gain is selected based on a specified open-loop bandwidth ω_b. The proportional gain is chosen as

$$k_p = \left|\frac{1}{G_d(s)}\right|_{\omega=\omega_b}. \tag{43}$$

The choice of the desired bandwidth ω_b is critical for satisfying the required gain margin (GM) and phase margin (PM) specifications for robustness, namely

$$\begin{aligned} &\text{GM} \geq 6 \text{ dB}, \\ &\text{PM} \geq 60^\circ. \end{aligned} \tag{44}$$

Consequently, the outer open-loop transfer function $L(s)$ (with the inner closed-loop), mapping from the reference input r to the output y, is expressed as

$$\begin{aligned} L(s) &= k_p \cdot G_d(s) \\ &= k_p \cdot \frac{G(s)}{1 + G(s)C_d(s)} \\ &= k_p \cdot \frac{\omega_n^2(s+\omega_a)}{s\left(s^2 + \omega_a s + 2\omega_n^2\right)}, \end{aligned} \tag{45}$$

where $k_p = \left|G_d(s)^{-1}\right|_{\omega=\omega_b}$. Thus, at the 0 dB crossover frequency ω_b, it holds that $|L(s)|_{\omega=\omega_b} = 1$. The phase of $L(s)$ at ω_b can then be simplified and expressed as

$$\angle L(s)_{\omega=\omega_b} = \tan^{-1}\left(\frac{\omega_b}{\omega_a}\right) - \frac{\pi}{2} - \tan^{-1}\left(\frac{\omega_a\omega_b}{2\omega_n^2 - \omega_b^2}\right). \tag{46}$$

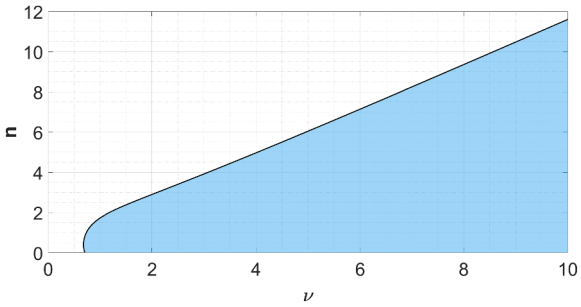

Fig. 17. Illustration of the solution space (shaded light blue) to tune n for a specific ν to ensure a 60° phase margin.

Using $\nu = \omega_n/\omega_b$ and $n = \omega_a/\omega_n$ to normalize (46) and enforcing PM $\geq 60^\circ$ allows the condition to be rewritten as

$$\tan 60^\circ \leq \frac{n \cdot 2\nu^3}{n^2\nu^2 - 2\nu^2 + 1}. \tag{47}$$

For a selected ω_b (and thus ν), the parameter n can be tuned to satisfy the above inequality. The corresponding feasible region in the (ν, n)-plane is illustrated in Fig. 17 and is defined by

$$1.75\nu^2n^2 - 2\nu^3 n + 1.75\left(1 - 2\nu^2\right) \leq 0. \tag{48}$$

From this relation, it can be inferred that, to obtain a high ω_b (or low ν), a lower n must be chosen, leading to a trade-off in the achievable damping performance.

4.1.2. Integrator requirement in tracking controller

Eq. (23) shows that perfectly matching the controller gain with the plant's DC gain causes an integrator effect by placing a pole at zero in the inner closed-loop ($p_1 = 0$). However, exact gain matching is impractical due to limited numerical precision in discrete-time controller implementations.

For an undamped second-order system, assume that an NRC is tuned so that the controller gain is $k' = k + \Delta k$, where $\Delta k < 0$ is infinitesimally small compared to unity but not zero ($|\Delta k| \approx 0$). Note that for $\gamma = 1$ and $\Delta k > 0$, $C_d(s)$ becomes unstable, requiring careful tuning with $\gamma \lessapprox 1$ in practice. Consequently, $C_d'(s) = k'(s - \omega_a)/(s + \omega_a)$. Then, the inner closed-loop function from d to y can be expressed as

$$\begin{aligned} G_d'(s) &= \frac{G(s)}{1 + G(s)C_d'(s)} \\ &= \frac{\omega_n^2(s+\omega_a)}{s^3 + \omega_a s^2 + (2+\Delta k)\omega_n^2 s - \Delta k \omega_n^2 \omega_a}. \end{aligned} \tag{49}$$

When $|\Delta k| \neq 0$, the closed-loop characteristic equation has a small finite root instead of $s = 0$. Therefore, when $C_t(s) = k_p$, the dual closed-loop system cannot achieve zero steady-state error. Mathematically, for a reference input r, the Laplace domain representation of the error e can be written as

$$\begin{aligned} E(s) &= R(s) - Y(s) \\ &= \frac{1 + G(s)C_d(s)}{1 + G(s)(C_t(s) + C_d(s))} R(s). \end{aligned} \tag{50}$$

The steady-state error e_{ss} for a step reference input ($R(s) = 1/s$) is then given by the final value theorem as

$$e_{ss} = \lim_{s\to 0} sE(s) = \frac{2}{2 + k_p} \neq 0, \tag{51}$$

where

$$k_p = \left|G_d^{-1}(s)\right|_{\omega=\omega_b} \approx \left|\frac{\omega_n^2 - \omega_b^2}{\omega_n^2}\right|. \tag{52}$$

If the inner closed-loop lacks an exact integrator, the tracking controller must incorporate one to ensure zero steady-state error in the dual

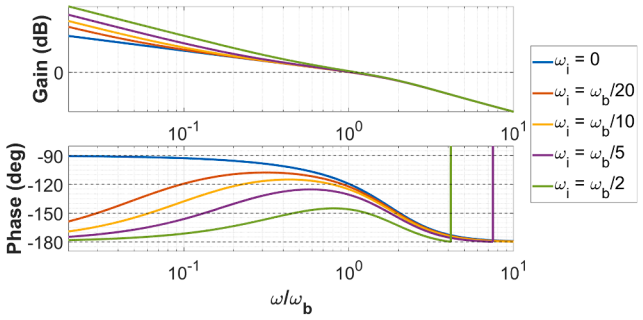

Fig. 18. Influence of the integrator frequency ω_i on the open-loop stability margins of $L(s)$.

closed-loop system. In this case, the tracking controller $C_t(s)$ is given by (42), but the integrator can have a very small corner frequency.

Fig. 18 illustrates the impact of the integrator corner frequency ω_i on the open-loop phase margin, following the tuning guidelines outlined above. As ω_i increases relative to the tuned open-loop bandwidth ω_b, the phase lag introduced by the integrator becomes more pronounced, reducing the phase margin evaluated at ω_b. At the same time, this increase in ω_i also results in higher loop gains, as depicted in the magnitude plot, which helps to achieve better disturbance rejection (objective O_2 in (15)). However, a trade-off arises, since higher ω_i can lead to a violation of upper bounds for dual closed-loop bandwidths (such as ±1 dB or ±3 dB) due to lower phase margins, as illustrated in the following section. For this illustration, the following parameters are chosen: $\nu \approx 1.33$ and $n = 2.2$ (resulting in a sufficiently damped resonance), which will also be used in the subsequent study.

4.2. Dual closed-loop shaped sensitivities

In this section, different dual closed-loop transfer functions are illustrated for the proposed control architecture with a conventional PI controller $C_t(s)$ and the NRC $C_d(s)$ in feedback. The tuning of each controller follows the guidelines elaborated in Sections 3.1 and 4.1.

The purpose of employing the NRC is to completely damp the resonance peak and enable the dual closed-loop system to achieve high bandwidths. Fig. 19(a) shows the dual closed-loop frequency response $T_{yr}(s)$ for a second-order system incorporating this control architecture and the associated tuning guidelines. The effect of the integrator frequency ω_i within $C_t(s)$ is included for demonstration. As ω_i increases, it can be observed that the dual closed-loop bandwidth ω_c (defined via the ±1 dB or ±3 dB bounds around 0 dB) may be reduced or these bounds may be violated. Therefore, to meet stringent closed-loop tracking performance requirements, it is advisable to use an integrator with a relatively low ω_i to ensure zero steady-state error, while the high loop gain requirement is primarily provided by the integrator effect of the inner closed-loop. It should be emphasized that, with suitable tuning of ν and n, it is possible to achieve a dual closed-loop bandwidth ω_c (for both ±1 dB and ±3 dB bounds) that is higher than the first resonance frequency ω_n of the system ($\omega_c > \omega_n$). This, however, comes at the expense of not achieving complete damping of the resonance peak, although the peak remains sufficiently well damped for practical purposes.

In the complementary function $T'_{xr}(s)$ (Fig. 19(b)), it is observed that even without a pronounced integrator in the outer loop, lower sensitivity gains are achieved at low frequencies. This is primarily due to the tuning of NRC to achieve $|G(s)C_d(s)| = 1$ and $\angle G(s)C_d(s) = \pi$ for $\omega \ll \omega_a$, as discussed in Section 3.1.2. In contrast, for the conventional case (Fig. 3(a)), attenuation is limited to a smaller range of frequencies due to lower bandwidths. The proposed method can further enhance this performance by slightly increasing ω_i of the outer-loop integrator, achieving even lower gains at low frequencies. However, it is crucial to tune this parameter carefully to balance the trade-offs with other

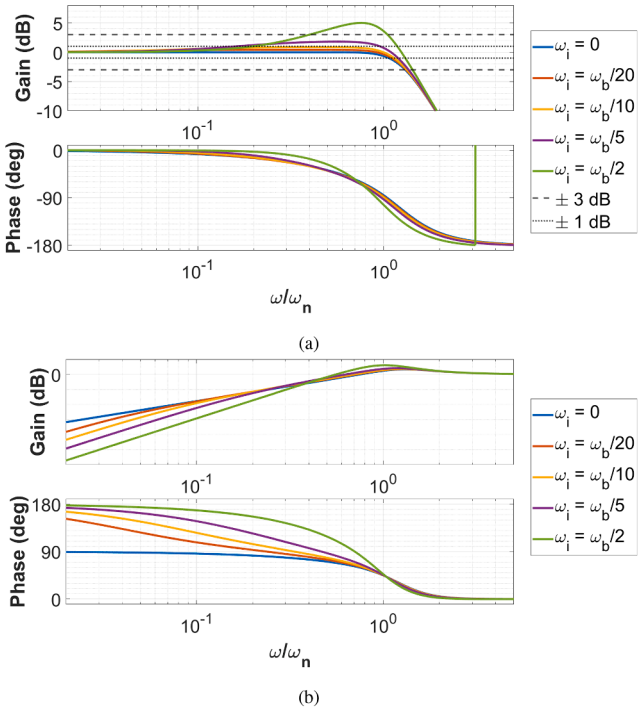

Fig. 19. Illustration of dual closed-loop frequency response as ω_i varies: (a) $T_{yr}(s) : r \mapsto y$, (b) $T'_{xr}(s) : r \mapsto e_r$.

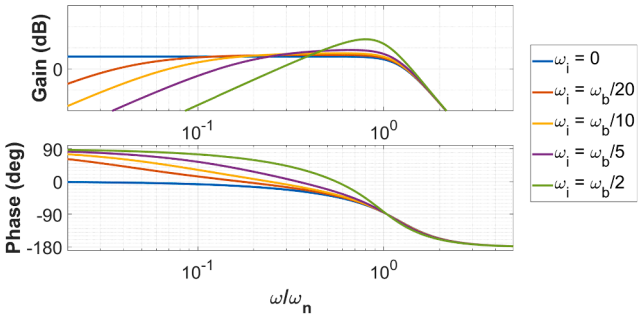

Fig. 20. Illustration of the dual closed-loop frequency response $PS_{yd}(s) : d \mapsto y$ (or x or e_r) as ω_i varies.

sensitivity function gains at relevant frequencies, as highlighted in Section 2.3.

Although tracking performance in the frequency domain is illustrated in Fig. 19, it is also crucial to understand how loop tuning impacts disturbance rejection and noise attenuation in the frequency domain. Typically, noise dominates at high frequencies, while process disturbances can span from low to high frequencies, depending on the system, its environmental conditions, and the specific application. Additionally, internal couplings within the system often introduce disturbances to the motion axis being controlled, particularly at the system's resonance frequencies. Consequently, reducing the sensitivity gains at the relevant frequencies is essential, with a particular focus on the problematic frequency regimes.

The effect of NRC in providing a well-damped response is evident from the flat gain in the process sensitivity function $PS_{yd}(s)$ around the resonance frequency, as illustrated in Fig. 20. However, the integrator effect provided by the inner closed loop does not offer any particular advantage at low frequencies with respect to disturbance rejection. This could be a concern in applications where the system is subject to low-frequency disturbances, such as floor vibrations. As shown in Fig. 20, the process sensitivity gains at low frequencies can be significantly reduced

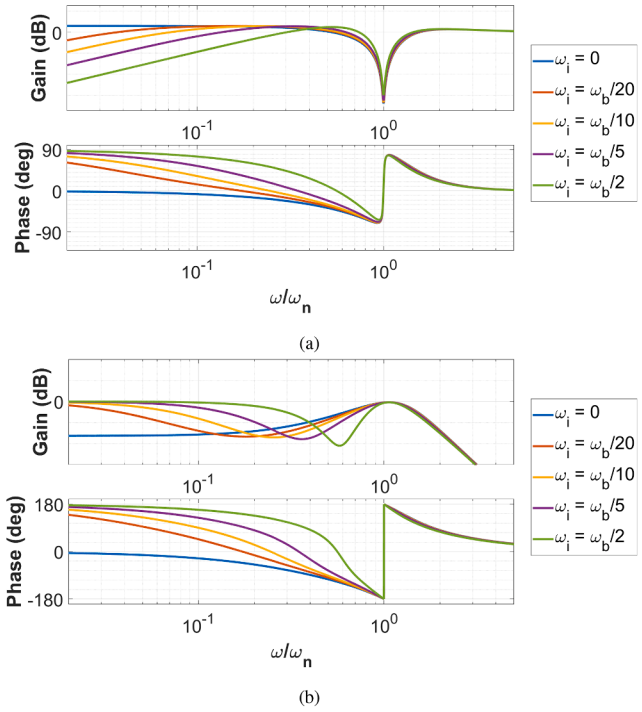

Fig. 21. Illustration of dual closed-loop frequency response as ω_i varies: (a) $S_{yn}(s) : n \mapsto y$, (b) $S_{xr}(s) : n \mapsto e_r$.

by incorporating a more pronounced integrator in the outer tracking loop. As discussed earlier, this adjustment comes at the expense of reduced dual closed-loop bandwidth.

Similarly, in the noise sensitivity function $S_{yn}(s)$, a deep notch-like behavior indicates substantial noise attenuation near the resonance frequencies, implying a reduced influence of noise on the measured position y. Again, the low-frequency sensitivity gains can be decreased with a higher integrator corner frequency ω_i, if necessary (Fig. 21(a)). However, when evaluating the influence of noise n on the real error e_r via $S_{xr}(s)$, it can be observed that, even with a pronounced integrator, the low-frequency noise attenuation is not significant (Fig. 21(b)). This follows from the inherent limitations of linear control, as highlighted in Section 2.3. In practice, this is typically not an issue, since noise tends to dominate at high frequencies, where the system gains naturally roll off.

Thus, this section highlights the importance of shaping these dual closed-loop sensitivity functions to minimize the real error within the controlled system. By combining the advantages of the proposed control method with the known limitations of linear control theory, there is considerable flexibility to effectively balance the trade-offs between achievable damping and reference tracking, disturbance rejection, and noise attenuation over the relevant frequency ranges.

4.3. Controller tuning guidelines

This subsection summarizes the controller tuning process and provides general guidelines, illustrated in Fig. 22, to be followed for tuning the controllers.

5. Experimental setup and results

This section presents the experimental setup, which incorporates the industrial nanopositioning system, to experimentally demonstrate the damping performance of the proposed NRC and the dual closed-loop performance achieved by shaping different sensitivity functions.

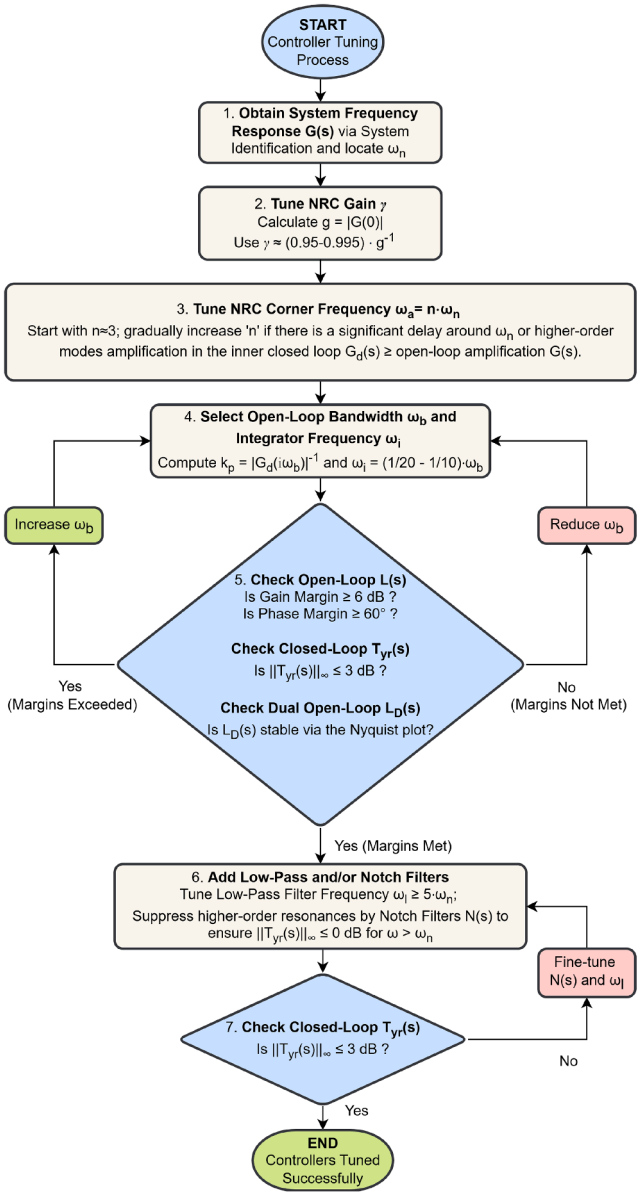

Fig. 22. Controller tuning guidelines for dual closed-loop framework.

5.1. System description

Presented in Fig. 23, the experimental setup utilizes a commercial P-621.1CD PIHera linear precision nanopositioner with a travel range of 100 μm. The single-axis positioning stage incorporates a ceramic-insulated multilayer piezo-stack actuator, a flexure-based mechanism-guided platform, and a high-resolution capacitive sensor. The stage utilizes a voltage amplifier and sensor signal conditioning modules integrated within the modular E-712 piezo-controller. The commercial hardware is integrated with an NI CompactRio chassis with an embedded FPGA, facilitating actuation signals and control for external control. The chassis includes 16-bit analog input-output modules that enable transmission and reception of signals to implement the control approach. The control scheme is implemented using the NI LabVIEW software, which interfaces the host computer and the nanopositioner. The actuation voltage ranges from 0 to 10 V, and the sampling time t_s of the FPGA-based control loop is set to 30 μs. The high sampling frequency $f_s = 33.\overline{33}$ kHz yields a Nyquist frequency of approximately 16.66 kHz, which is more than six times higher than the frequency range of interest (0-3000 Hz)

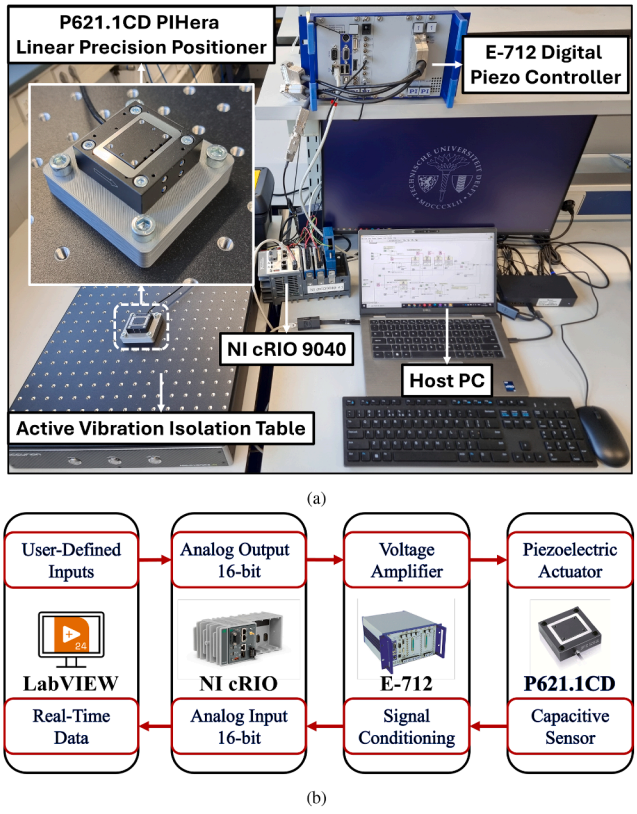

Fig. 23. Experimental setup of a piezo-actuated nanopositioning system (a) Experimental platform (b) System workflow.

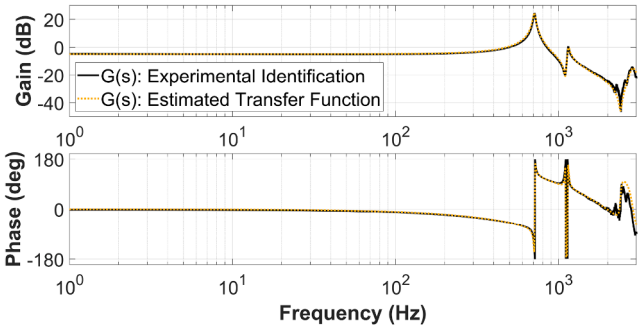

Fig. 24. Identified frequency response of the nanopositioning system $G(s)$.

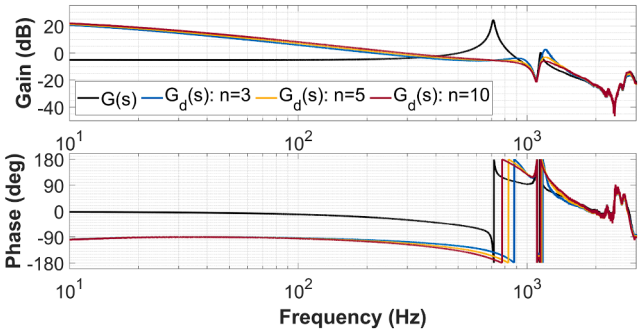

Fig. 25. Experimentally identified inner closed-loop frequency response $G_d(s)$.

for system identification and control. For controller implementation, the bilinear transform (Tustin discretization) is employed. The FPGA implementation uses a 64-bit double-precision floating-point numerical data type in LabVIEW, providing approximately 15 decimal digits of accuracy to ensure precise discrete-time control implementation. Furthermore, the LabVIEW program is optimized to guarantee that the FPGA loop rate matches the sampling rate, thereby preventing any data loss. The synthesized FPGA design occupies a total of 9608 slices, comprising 30,780 slice registers and 22,820 slice look-up tables (LUTs), and additionally utilizes 8 Block RAMs and 129 DSP48 digital signal processing units.

5.2. System identification

A sinusoidal chirp signal (0.75 to 1 V) was generated with LabVIEW and sent to the piezo-actuator for system identification. The capacitive sensor measured the position output, and the input-output signals were imported into MATLAB for analysis. The transfer functions were estimated using MATLAB's signal processing toolbox. A high sampling frequency F_s of 33.3 kHz provided sufficient data for accurate identification.

The dominant resonance peak ω_n is at 710 Hz, with the second mode ω_2 nearby at 1150 Hz (see Fig. 24). A notable phase delay occurs due to actuator-amplifier dynamics and system time delay, even at frequencies below ω_n. Higher modes appear around and beyond 2000 Hz. Pole-zero interlacing indicates the system's collocated nature.

5.3. Experimental inner closed-Loop frequency response

With the identified system frequency response of the piezoelectric nanopositioning stage, the NRC is designed and implemented to dampen the dominant resonance and extend the system bandwidth. According to the design guidelines presented in Section 3.1, a normalized corner frequency of $n \approx 3$ should ensure complete damping of the resonance peak. However, due to the significant phase lag occurring below ω_n, n is re-tuned to achieve a sufficiently damped peak (see Section 3.1.5). Implementing the NRC also provides damping in nearby higher-order modes (see Section 3.3). As shown in Fig. 25, while the dominant resonance is effectively suppressed, the second mode at $\omega_2 = 1150$ Hz also exhibits noticeable damping, which increases as n increases. For $n = 10$, the second resonance peak is reduced by approximately 6 dB. It should be emphasized that this increase in n comes at the cost of an additional phase delay for $\omega \leq \omega_n$. This additional phase lag must be carefully considered during the tuning process to ensure that the tracking controller preserves the required stability margins.

Thus, based on the corner frequency tuning shown in Fig. 25 and the controller gain derived from (22), the damping controller is implemented with $n = 10$ and $k = 1.7658$ (for $\gamma = 0.995$). Owing to the high resolution of the capacitive sensor, analog modules, and ADC/DAC conversion, the taming of NRC is not implemented in this work.

5.4. Experimental dual closed-loop frequency response

In this dual closed-loop control approach, a feedback tracking controller handles tracking errors. As discussed previously, a proportional-integral (PI) controller is designed based on the inner closed-loop dynamics ($G_d(s)$) to achieve the highest possible dual closed-loop bandwidths. However, in practical systems like this, higher-order modes, if not adequately suppressed, can lead to significant closed-loop gains at their corresponding frequencies. Furthermore, high-frequency noise is a common issue that must be attenuated. To address these challenges, the tracking controller, in this case, is designed as a series combination of a PI controller, a notch filter targeting the dominant higher-order mode, respectively, and a low-pass filter to mitigate high-frequency noise.

The implemented tracking controller $C_t(s)$ is expressed as follows:

$$C_t(s) = \underbrace{k_p \cdot \left(1 + \frac{\omega_i}{s}\right)}_{\substack{\text{Proportional} \\ \text{Integral Term}}} \cdot \underbrace{N(s)}_{\substack{\text{Notch} \\ \text{Filter}}} \cdot \underbrace{\left(\frac{\omega_l}{s + \omega_l}\right)}_{\substack{\text{Low-Pass} \\ \text{Filter}}}, \tag{53}$$

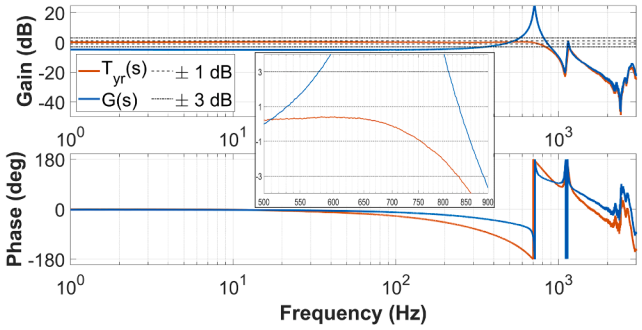

Fig. 26. Experimentally identified dual closed-loop frequency response $T_{yr}(s)$.

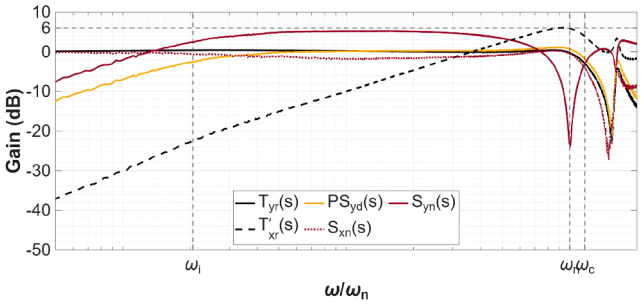

Fig. 27. Experimentally identified $(T_{yr}(s), PS_{yd}(s), S_{yn}(s))$ and estimated $(T'_{xr}(s), S_{xn}(s))$ dual closed-loop sensitivities.

where the notch filter $N(s)$ is as follows:

$$N(s) = \left(\frac{(\frac{s}{\omega_{N_1}})^2 + (\frac{s}{Q_1 \omega_{N_1}}) + 1}{(\frac{s}{\omega_{N_1}})^2 + (\frac{s}{Q_2 \omega_{N_1}}) + 1} \right) \tag{54}$$

The tracking controller is tuned to achieve an open-loop bandwidth ω_b of 282 Hz, with gain and phase margins of 6 dB and 59°, respectively, ensuring sufficient robustness. The tuning parameters are as follows: $k_p = 0.9722$, $\omega_i = 14.6$ Hz, $\omega_{N_1} = 1250$ Hz, $\omega_l = 5000$ Hz, $Q_1 = 1.2$, $Q_2 = 1$. The parameters of the notch filter are designed to achieve sufficient attenuation of the higher-order resonance at the shifted closed-loop resonant frequency, while avoiding degradation of the control bandwidths due to excessive phase lag introduced by the filter. For dual closed-loop stability, the phase margins ϕ_{m_i} at all crossover frequencies $\omega_{cf_i} \mid |L_D(\omega_{cf_i})| = 1$ are evaluated and validated.

After implementing the tuned controllers, the dual closed-loop frequency response $T_{yr}(s)$ is experimentally estimated through a closed-loop system identification process, as shown in Fig. 26, where it can be observed that both the crossings ±1 dB and ±3 dB occur beyond the resonance frequency $\omega_n = 710$ Hz, specifically at 755 Hz and 830 Hz (ω_c), respectively. These experimental results clearly show that effectively tuning the dual closed-loop incorporating the proposed NRC enables the system to achieve dual closed-loop bandwidths that surpass the dominant resonance frequency.

5.5. Experimental dual closed-loop sensitivities

This subsection reflects on experimentally identified sensitivities to dual closed-loop shaping guidelines (see Section 2.3) and those shaped using the proposed NRC (see Section 4.2). The experimental sensitivity magnitudes are shown in Fig. 27. It is crucial to assess the impact of input signals r, d, and n on both the measured position y and the real error e_r in the dual closed-loop system. Sensitivities are shaped to minimize the impact of these signals on e_r in relevant frequency regimes.

As shown in Fig. 26, ω_c exceeds ω_n, aided by the NRC ($C_d(s)$) tuning, so that $|G(s)C_d(s)| = 1$ and $\angle G(s)C_d(s) \approx \pi$ up to $\omega \approx \omega_{C_d}$. The 0 dB crossing of $T'_{xr}(s)$ near ω_{C_d} implies minimal influence of r on e_r for $\omega < \omega_{C_d}$.

The NRC ensures a well-dampened peak, as shown by flat gains around ω_n in the process sensitivity function $PS_{yd}(s)$. To reduce the low-frequency gains of $PS_{yd}(s)$ and ensure zero steady-state tracking, the integrator in $C_t(s)$ is tuned according to $\omega_i = \omega_b/20$. Increasing ω_i decreases ω_c and slightly amplifies the dynamics around ω_n. The system's high-frequency gain roll-off and low-pass filter in $C_t(s)$ ensures sufficiently low gains for $S_{xn}(s)$. However, limitations in Section 2.3 prevent attenuation of contributions of n to e_r at low frequencies. The experimental findings align with the guidelines and analysis presented in this paper.

5.6. Experimental evaluation against benchmark methods

This subsection elaborates upon the preceding subsection by providing an experimental evaluation that demonstrates the efficacy of the proposed method in comparison to benchmark methods. Two specific cases are considered for this benchmarking process: (1) a classical single-loop control architecture (see Fig. 3(a)), wherein the tracking controller $C_t(s)$ comprises a series configuration of a standard Proportional-Integral (PI) controller and two notch filters designed to suppress the two primary resonant peaks, and (2) a dual closed-loop control architecture akin to that of the proposed method, wherein a widely utilized positive position feedback (PPF) controller is employed for active damping. It is noteworthy that the majority of active damping controllers documented in the literature adhere to a loop-shaping methodology analogous to that of PPF.

As illustrated in Fig. 28(a), which corresponds to the closed-loop frequency response $T_{yr}(s)$, the attained ±3 dB closed-loop bandwidth for the PI + NRC configuration (830 Hz) significantly surpasses those achieved with the PI + Notch (153 Hz) and PI + PPF (274 Hz) configurations, respectively. This result clearly indicates the capability to accurately track reference signals at frequencies exceeding the system's resonance frequency, whereas in alternative configurations, this capability is confined to a fraction of the system's resonance frequency.

Furthermore, Fig. 28(b) presents the closed-loop frequency response $PS_{yd}(s)$, comparing the three cases. It is apparent that in the case involving PI + Notch, the method does not succeed in suppressing the resonance frequency, thereby highlighting its ineffectiveness in rejecting disturbances around that frequency. The PI + PPF scenario performs comparatively well by providing a reasonable level of attenuation at the peak frequency. The PI + NRC scenario, in contrast, exhibits a flat response at that frequency, demonstrating its ability to completely dampen the resonance mode and reject disturbances around the resonance frequency. Nevertheless, this performance incurs a trade-off at lower frequencies, where the attenuation is reduced compared to the other two scenarios. This phenomenon arises because, in this case, a very low integrator frequency ω_i is applied to optimize ω_c. As alluded to in the preceding sections, based on the system requirements and the frequency distribution of deterministic disturbances, this low-frequency performance can be traded off against peak attenuation at ω_n in $PS_{yd}(s)$ to a significant extent. One possible approach would be to increase the integrator gain in the tracking controller or to employ an inversion-based feedforward controller to enhance sensitivity at low frequencies. The potential integration of disturbance observers in combination with damping controllers could also be investigated; however, this lies beyond the scope of the present work.

5.7. Reference tracking time-domain performance

The nanopositioning stage aims to accurately follow predefined trajectories, typically periodic ones. Fig. 26 shows its ability to track references up to dual closed-loop bandwidths in the frequency domain. This

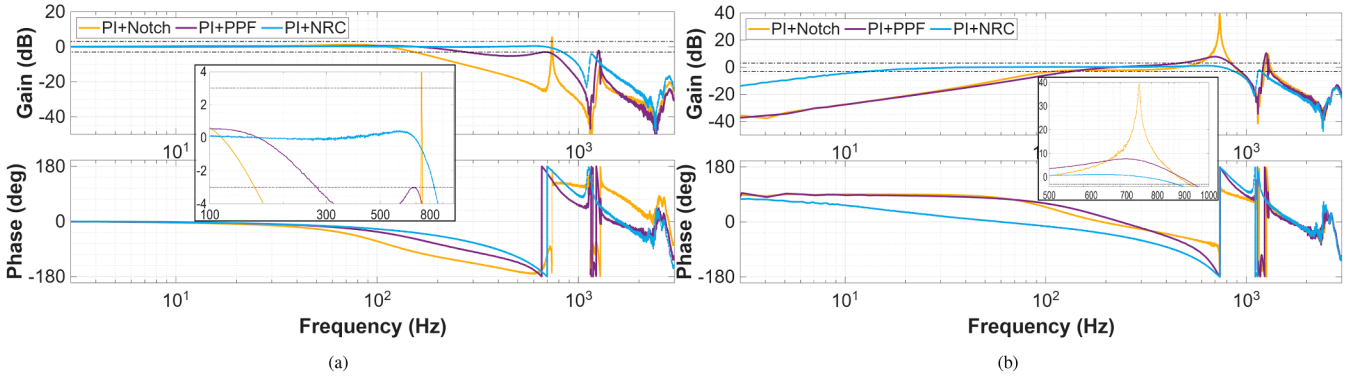

Fig. 28. Experimental frequency response comparison of measured sensitivities: (a) $T_{yr}(s)$, and (b) $PS_{yd}(s)$, with benchmark methods.

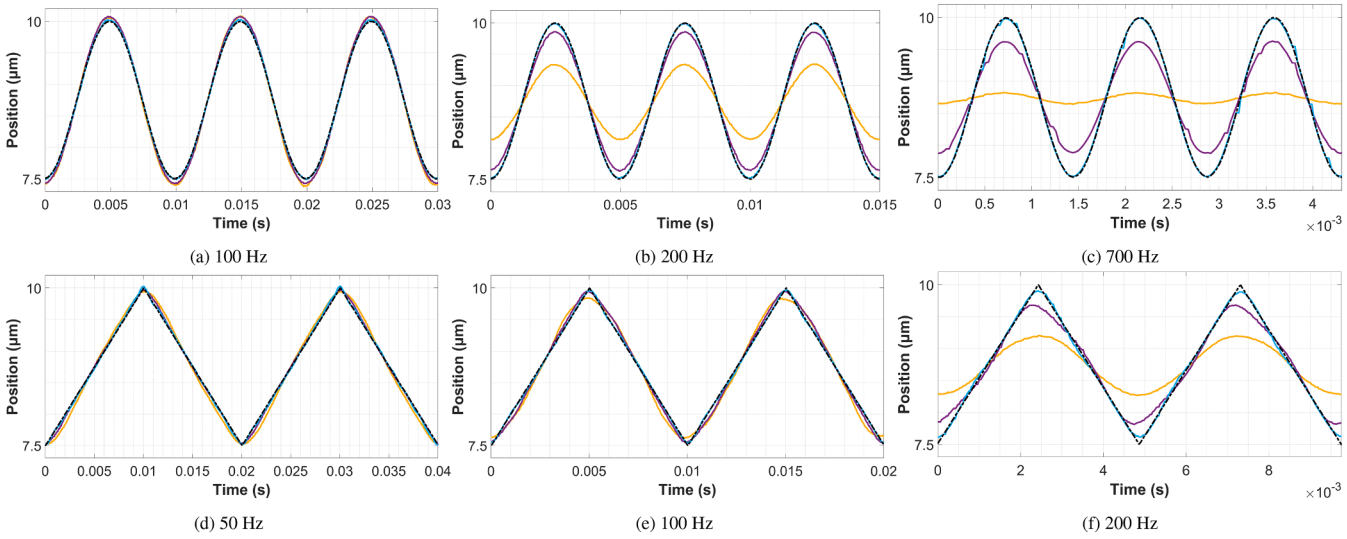

Fig. 29. Reference tracking performance for sinusoidal inputs (a-c) and triangular inputs (d-f) at selected frequencies. Each subplot illustrates the reference signal (- · -), the measured output using PI + Notch control (——), PI + PPF control (——), and PI + NRC control (——).

Table 1
Comparison of tracking performance for different inputs and frequencies.

Frequency (Hz)	Sinusoidal						Triangular					
	PI + Notch		PI + PPF		PI + NRC		PI + Notch		PI + PPF		PI + NRC	
	e_{max}	e_{rms}	e_{max}	e_{rms}	e_{max}	e_{rms}	e_{max}	e_{rms}	e_{max}	e_{rms}	e_{max}	e_{rms}
1	0.062	0.019	0.126	0.048	0.055	0.014	0.051	0.018	0.107	0.047	0.057	0.013
2	0.062	0.022	0.107	0.041	0.060	0.014	0.057	0.021	0.094	0.039	0.055	0.013
5	0.047	0.017	0.087	0.030	0.077	0.022	0.061	0.017	0.077	0.030	0.082	0.020
10	0.047	0.018	0.033	0.008	0.084	0.035	0.076	0.019	0.040	0.008	0.102	0.030
20	0.077	0.026	0.040	0.010	0.101	0.044	0.115	0.032	0.055	0.012	0.091	0.036
50	0.164	0.089	0.064	0.029	0.091	0.035	0.198	0.086	0.098	0.032	0.077	0.026
100	0.144	0.068	0.113	0.061	0.080	0.024	0.193	0.096	0.142	0.060	0.077	0.022
200	0.697	0.459	0.187	0.106	0.104	0.024	0.838	0.400	0.347	0.126	0.150	0.040
300	0.960	0.649	0.454	0.304	0.189	0.068	1.019	0.532	0.572	0.255	0.226	0.082
400	1.077	0.729	0.590	0.395	0.252	0.091	1.121	0.605	0.728	0.341	0.202	0.082
500	1.145	0.778	0.621	0.401	0.212	0.058	1.185	0.644	0.723	0.338	0.255	0.090
600	1.189	0.813	0.572	0.347	0.369	0.148	1.204	0.665	0.704	0.307	0.325	0.129
700	1.204	0.822	0.468	0.272	0.324	0.114	1.238	0.690	0.590	0.231	0.272	0.101
800	1.155	0.788	0.748	0.470	0.475	0.245	1.199	0.660	0.899	0.432	0.535	0.229

section evaluates time-domain performance, with the system subjected to sinusoidal and triangular references, with frequencies spanning from 1 to 800 Hz.

It is important to note that the phase lag increases with increasing frequencies in the dual closed-loop system. Perfectly delayed tracking is often implemented in typical periodic scanning applications, provided the delay is well known. Thus, phase lags are removed using post-processing techniques to reasonably represent the tracking performance. The known phase lag ϕ_l (in degrees) at the corresponding frequency f (in Hz) is utilized to compute the resulting time delay t_d, given by:

$$t_d = \frac{\phi_l}{f \cdot 360}. \tag{55}$$

Subsequently, the shifted outputs $y^*(t)$ can be computed as follows:

$$y^*(t) = y(t_{i+N_d} : t_N) \text{ for } i = [1, N] \text{ and } i \in \mathbb{Z}. \tag{56}$$

In discrete time, phase lags are compensated by shifting $N_d = \lfloor |t_d|/t_s \rceil$ samples, where t_s is the sampling time, and $\lfloor \cdot \rceil$ is the round function. Fig. 29 shows the phase-corrected system tracking response for amplitude references from 7.5 μm to 10 μm.

To assess the tracking performance, we consider two common indices: the maximum tracking error (e_{max}) and the root mean square tracking error (e_{rms}).

$$e_{max} = \max\left(\left|y(t_i) - r(t_i)\right|\right), \tag{57}$$

$$e_{rms} = \sqrt{\frac{1}{N}\sum_{i=1}^{N}\left(y(t_i) - r(t_i)\right)^2}, \tag{58}$$

where $r(t_i)$ and $y(t_i)$ represents the reference signal and output signal at discrete time step i, respectively, and N is the total number of samples, with $i = 1, 2, 3, \ldots, N$.

Table 1 illustrates the calculated tracking errors, facilitating a comparison between the two benchmark methods and the proposed NRC-based method. The results indicate that the system achieves minimal errors for reference signals up to 800 Hz in the proposed method, whereas alternative methods are only capable of accurate tracking within the limits of their respective closed-loop bandwidth frequencies. However, performance degrades for frequencies beyond this point, aligning with the drop in sensitivity gains as frequencies exceed the dual closed-loop bandwidth ω_c. It is important to note that these error magnitudes can vary depending on the actual tuning of all controller parameters, which are adjusted based on specific application requirements. The presented values indicate the system's tracking capabilities up to ω_c.

6. Conclusions

This paper introduces a novel Non-Minimum-Phase Resonant Controller (NRC) tailored for active damping control in dual-closed-loop architectures, applied to piezo-actuated nanopositioning systems. The NRC leverages non-minimum-phase characteristics to achieve complete damping and the bifurcation of the double resonant poles of the primary resonance peak through a constant-gain design with a tunable phase, ensuring robustness even under varying load conditions. In addition, the paper demonstrates the controller's capability to dampen higher-order flexural modes. In alignment with the dual closed-loop shaping guidelines delineated in this paper, the proposed NRC can provide high gains at low frequencies within the inner loop, which, complemented by a standard PI tracking controller, facilitates the system to achieve high dual closed-loop bandwidths that potentially surpass the primary resonance frequency. Furthermore, the NRC minimizes the impact of low-frequency reference signals on real feedback errors and ensures robust disturbance rejection near the resonance frequency. Experimental results validate NRC performance, demonstrating dual closed-loop bandwidths of 830 Hz and 755 Hz (within ±3 dB and ±1 dB bounds, respectively) that exceed the first resonance frequency at 710 Hz, even amidst significant system delay, a performance level unattainable with the benchmarked methods employed for comparison. These outcomes underscore the potential of the NRC for high-performance, precise nanopositioning applications.

CRediT authorship contribution statement

Aditya Natu: Writing – review & editing, Writing – original draft, Visualization, Validation, Software, Project administration, Methodology, Investigation, Formal analysis, Data curation, Conceptualization; **Hassan Hosseinnia:** Writing – review & editing, Validation, Supervision, Resources, Methodology, Investigation, Funding acquisition, Formal analysis, Conceptualization.

Data availability

Data will be made available on request.

Declaration of competing interest

The authors declare that they have no known competing financial interests or personal relationships that could have appeared to influence the work reported in this paper.

Acknowledgments

This work was financed by Physik Instrumente (PI) SE & Co. KG and co-financed by Holland High Tech with PPS Project supplement for research and development in the field of High Tech Systems and Materials.

The authors express their sincere gratitude to both Mathias Winter, Head of Piezo System & Drive Technology, and Dr.-Ing. Simon Kapelke, Head of Piezo Fundamental Technology, from Physik Instrumente (PI) SE & Co. KG, for their invaluable collaboration in providing technical insights concerning the system and its applications.

References

Abramovitch, D. Y., Hoen, S., & Workman, R. (2008). Semi-automatic tuning of PID gains for atomic force microscopes. In *2008 American control conference* (pp. 2684–2689). IEEE.

Al-Mamun, A., Keikha, E., Bhatia, C. S., & Lee, T. H. (2013). Integral resonant control for suppression of resonance in piezoelectric micro-actuator used in precision servomechanism. *Mechatronics*, *23*(1), 1–9.

Åström, K. J., & Murray, R. (2021). Feedback systems: An introduction for scientists and engineers. Princeton university press.

Babarinde, A. K., Zhu, L.-M., & Aphale, S. S. (2019). Simultaneous design of positive acceleration velocity and position feedback based combined damping and tracking control scheme for nanopositioners. In *2019 18th european control conference (ECC)* (pp. 608–613). IEEE.

Chen, Z., Zhong, X., Shi, J., & Zhang, X. (2021). Damping-enabling technologies for broadband control of piezo-stages: A survey. *Annual Reviews in Control*, *52*, 120–134.

Clayton, G. M., & Devasia, S. (2009). Conditions for image-based identification of SPM-nanopositioner dynamics. *IEEE/ASME Transactions on Mechatronics*, *14*(4), 405–413.

Das, S. K., Pota, H. R., & Petersen, I. R. (2014). A MIMO double resonant controller design for nanopositioners. *IEEE Transactions on Nanotechnology*, *14*(2), 224–237.

Dastjerdi, A. A., Saikumar, N., & HosseinNia, S. H. (2018). Tuning guidelines for fractional order PID controllers: Rules of thumb. *Mechatronics*, *56*, 26–36.

Devasia, S., Eleftheriou, E., & Moheimani, S. O. R. (2007). A survey of control issues in nanopositioning. *IEEE Transactions on Control Systems Technology*, *15*(5), 802–823.

Feng, H., Pang, A., & Zhou, H. (2022). High precision robust control design of piezoelectric nanopositioning platform. *Scientific Reports*, *12*(1), 10357.

Feng, H., Zhou, H., Jiang, C., & Pang, A. (2023). High precision structured h control of a piezoelectric nanopositioning platform. *PloS One*, *18*(6), e0286471.

Feng, Z., Ling, J., Ming, M., & Xiao, X.-H. (2017). High-bandwidth and flexible tracking control for precision motion with application to a piezo nanopositioner. *Review of Scientific Instruments*, *88*(8).

Fleming, A. J. (2009). Nanopositioning system with force feedback for high-performance tracking and vibration control. *IEEE/ASME Transactions on Mechatronics*, *15*(3), 433–447.

Fleming, A. J., Aphale, S. S., & Moheimani, S. O. R. (2009). A new method for robust damping and tracking control of scanning probe microscope positioning stages. *IEEE Transactions on Nanotechnology*, *9*(4), 438–448.

Fleming, A. J., & Leang, K. K. (2014). Design, modeling and control of nanopositioning systems. Springer.

Gu, G.-Y., Zhu, L.-M., Su, C.-Y., Ding, H., & Fatikow, S. (2014). Modeling and control of piezo-actuated nanopositioning stages: A survey. *IEEE Transactions on Automation Science and Engineering*, *13*(1), 313–332.

Huang, W.-W., Wang, X., Meng, Y., Li, L., Zhang, X., Ren, M., & Zhu, L.-M. (2024). Design, modeling and control of high-bandwidth nano-positioning stages for ultra-precise measurement and manufacturing: A survey. *International Journal of Extreme Manufacturing*, *6*(6), 062007.

Hyun, C., Kaur, H., Rollings, R., Xiao, M., & Li, J. (2013). Threading immobilized DNA molecules through a solid-state nanopore at $>$ 100 μs per base rate. *ACS Nano*, *7*(7), 5892–5900.

Kaczmarek, M. B., & HosseinNia, H. (2023). Fractional-order negative position feedback for vibration attenuation. *Fractal and Fractional*, *7*(3), 222.

Lan, H., Ding, Y., Liu, H., & Lu, B. (2007). Review of the wafer stage for nanoimprint lithography. *Microelectronic Engineering*, *84*(4), 684–688.

Li, C.-X., Gu, G.-Y., Yang, M.-J., & Zhu, L.-M. (2015). Positive position feedback based high-speed tracking control of piezo-actuated nanopositioning stages. In *Intelligent robotics and applications: 8th international conference, ICIRA 2015, portsmouth, UK, august 24–27, 2015, proceedings, part II 8* (pp. 689–700). Springer.

Li, L., Li, C.-X., Gu, G., & Zhu, L.-M. (2017). Positive acceleration, velocity and position feedback based damping control approach for piezo-actuated nanopositioning stages. *Mechatronics*, *47*, 97–104.

Li, N., Wu, W., & Chou, S. Y. (2006). Sub-20-nm alignment in nanoimprint lithography using moire fringe. *Nano Letters*, *6*(11), 2626–2629.

Ling, J., Rakotondrabe, M., Feng, Z., Ming, M., & Xiao, X. (2019). A robust resonant controller for high-speed scanning of nanopositioners: Design and implementation. *IEEE Transactions on Control Systems Technology*, *28*(3), 1116–1123.

Maroufi, M., Bazaei, A., & Moheimani, S. O. R. (2014). A high-bandwidth MEMS nanopositioner for on-chip AFM: Design, characterization, and control. *IEEE Transactions on Control Systems Technology*, *23*(2), 504–512.

Moon, R. J., San-Millan, A., Aleyaasin, M., Feliu, V., & Aphale, S. S. (2017). Selection of positive position feedback controllers for damping and precision positioning applications. In *Modeling, design and simulation of systems: 17th asia simulation conference, asiasim 2017, melaka, malaysia, august 27–29, 2017, proceedings, part i 17* (pp. 289–301). Springer.

Rana, M. S., Pota, H. R., & Petersen, I. R. (2014). Performance of sinusoidal scanning with MPC in AFM imaging. *IEEE/ASME Transactions on Mechatronics*, *20*(1), 73–83.

Russell, D., Fleming, A. J., & Aphale, S. S. (2015). Simultaneous optimization of damping and tracking controller parameters via selective pole placement for enhanced positioning bandwidth of nanopositioners. *Journal of Dynamic Systems, Measurement, and Control*, *137*(10), 101004.

San-Millan, A., Russell, D., Feliu, V., & Aphale, S. S. (2015). A modified positive velocity and position feedback scheme with delay compensation for improved nanopositioning performance. *Smart Materials and Structures*, *24*(7), 075021.

Schmidt, R. M., Schitter, G., & Rankers, A. (2020). The design of high performance mechatronics-: high-Tech functionality by multidisciplinary system integration. Ios Press.

Shan, Y., & Leang, K. K. (2013). Design and control for high-speed nanopositioning: serial-kinematic nanopositioners and repetitive control for nanofabrication. *IEEE Control Systems Magazine*, *33*(6), 86–105.

Teo, Y. R., Russell, D., Aphale, S. S., & Fleming, A. J. (2014). Optimal integral force feedback and structured PI tracking control: Application for high speed confocal microscopy. *IFAC Proceedings Volumes*, *47*(3), 11793–11799.

Tuma, T., Sebastian, A., Lygeros, J., & Pantazi, A. (2013). The four pillars of nanopositioning for scanning probe microscopy: The position sensor, the scanning device, the feedback controller, and the reference trajectory. *IEEE Control Systems Magazine*, *33*(6), 68–85.

Wang, D., & Chen, X. (2017). A tutorial on loop-shaping control methodologies for precision positioning systems. *Advances in Mechanical Engineering*, *9*(12), 1687814017742824.

Yong, Y. K., Bhikkaji, B., & Moheimani, S. O. R. R. (2012a). Design, modeling, and FPAA-based control of a high-speed atomic force microscope nanopositioner. *IEEE/ASME Transactions on Mechatronics*, *18*(3), 1060–1071.

Yong, Y. K., Moheimani, S. O. R., Kenton, B. J., & Leang, K. K. (2012b). Invited review article: High-speed flexure-guided nanopositioning: Mechanical design and control issues. *Review of Scientific Instruments*, *83*(12).

Aditya Natu received the MSc in Mechanical Engineering (*cum laude*) with a specialization in Mechatronics System Design and is currently employed as a PhD Candidate at the Department of Precision and Microsystems Engineering, Delft University of Technology, Delft, The Netherlands. His research interests include active damping control, distributed actuation and sensing, precision mechatronics, and nanopositioning systems.

Dr. Hassan HosseinNia received his Ph.D. degree cum laude in Electrical Engineering in 2013, specializing in automatic control and its applications in mechatronics. He is currently a faculty member at Delft University of Technology (TU Delft), where he leads advanced research in precision mechatronic system design, high-performance motion control, active vibration damping, and the design and control of electromagnetic and piezoelectric actuators. His contributions have been recognized internationally. In 2024, he received the Abel Young Scientists Award from the 12th IFAC Conference on Fractional Differentiation and its Applications. His current research focuses on developing innovative control strategies and system architectures to enhance bandwidth and precision in next-generation mechatronic systems. He has published extensively in leading journals and conferences. Dr. HosseinNia served as the General Chair of the 7th IEEE International Conference on Control, Mechatronics, and Automation (ICCMA 2019). He also serves on the editorial boards of Mechatronics, Control Engineering Practice, and Fractional Calculus and Applied Analysis. Through his work, Dr. Hosseinnia brings a forward-looking perspective that bridges theoretical depth with industrial applicability, fostering innovation in advanced control and mechatronic system design.